Accurate and Computationally Efficient Nonlinear Static and Dynamic Analysis of Reinforced Concrete Structures Considering Damage Factors

Christos Mourlas[a], George Markou[b] and Manolis Papadrakakis[a]

[a]*Institute of Structural Analysis & Antiseismic Research, National Technical University of Athens, 9 Iroon Polytechniou Str.,Zografou Campus,GR-15780 Athens,Greece*
[b]*University of Pretoria, Department of Civil Enigneering, Pretoria, Republic of South Africa.*

Abstract

Accurate nonlinear dynamic analysis of reinforced concrete structures is necessary for estimating the behavior of concrete structures during an earthquake. A realistic modeling approach to assess their strength and their ability to carry the expected seismic forces is of great importance. Although a number of constitutive models and modeling approaches have been proposed in order to capture the behavior of reinforced concrete structures under static loading conditions, only a few of these numerical models have been extended to dynamic problems.
The objective of this paper is to integrate a computationally efficient 3D detailed modelling of concrete structures with damage factors that take into account the opening and closing of cracks, as well as, damage factors for steel reinforcement considering the surrounding concrete damage level, in order to capture the level of damage and stiffness degradation of structures undergoing many loading cycles.
In the adopted numerical model, the concrete domain is discretized with 8-noded isoparametric hexahedral finite elements, which treat cracking with the smeared crack approach, while the steel reinforcement is modeled as embedded beam elements inside the hexahedral mesh. The validity of the proposed method is demonstrated by comparing the numerical response with the corresponding experimental results of various reinforced concrete structural members and structures. Based on the numerical investigation, it was found that the proposed integration of the damage factors with computationally efficient concrete and steel material models can efficiently predict both static and dynamic nonlinear behavior of concrete structures, with the ability to capture the complicated phenomenon of the pinching effect.

Keywords: Nonlinear dynamic analysis; reinforced concrete; finite element method; 3D detailed modeling; damage factors

1. Introduction

The accurate numerical simulation of reinforced concrete (RC) structures under cyclic loading conditions has been a critical issue among many researchers over the last decades. Most constitutive material models are based on uniaxial laws with strain softening and tension stiffening characteristics. These models require many material parameters in order to capture the complex mechanical characteristics of concrete such as: micro-cracking, confinement, ductility, opening/closure of cracks and crushing. These studies indicate the necessity of a realistic constitutive law with parameters that have a direct physical meaning.

The complex behavior of RC structures under cyclic loading conditions makes the numerical procedure unstable, thus, it is more difficult to reach convergence when excessive cracking, rebar yielding and rebar rapture take place during the analysis. Therefore, a realistic 3D approach, which is characterized by simplicity and computational efficiency, is necessary in order to ensure accurate numerical simulations when trying to predict the carrying capacity of RC structures.

A detailed literature review on the modeling of the behavior of RC structures under cyclic loading conditions can be found in [1-3], where a limited number of numerical approaches can be

found implementing three-dimensional finite elements for the purposes of cyclic analysis. Pagnoni et al. [4] used 8-noded finite elements in conjunction with a 3D bounding surface which contains the possible stress points for a given damage level. Another approach for constitutive modelling was the use of various uniaxial relations on different planes called microplanes [5]. Eligehaousen et al. [6] used this approach in order to study 3D nonlinear analysis of beam-column RC joints emphasizing on bond-slip effects. Other researchers used the "equivalent uniaxial strain" concept, proposed by Darwin et al. [7], in order to combine the uniaxial laws with the biaxial or triaxial behavior of concrete. In this category, Balan et al. [8] studied the effect of concrete's post peak behavior due to the lateral confinement, Kwon et al. [9] proposed the coupling between deviatoric and volumetric stresses, whereas, Girard et al. [10] investigated the cyclic behavior of RC columns taking into account the bond-slip effect.

A number of researchers used the compression field theory to capture the behavior of RC members subjected mainly to shear stresses. Palermo and Vecchio [11] investigated the behavior of shear walls conducting 2D and 3D analysis under cyclic loading conditions. Belleti et al. [12, 13] proposed a unified approach based on the total strain fixed crack approach for reinforced concrete membrane elements indicating the essence of taking into account the shear resistance mechanisms that are developed along cracks. Furthermore, some models based on damage mechanics have been proposed for 3D cyclic analysis. Richard et al. [14] studied the characteristics of micro-cracking, sliding influence and partial stiffness recovery based on isotropic damage mechanics. Additionally, Jason et al. [15] combined an elastoplastic law with isotropic damage modelling in order to describe the hardening and softening behavior of concrete under cyclic compression. The model introduced many material parameters and illustrated the improvements achieved compared to a simple damage model but it was noted that the simulated responses were mesh-dependent. Yuchuan et al. [16] proposed an anisotropic damage model by using nonlinear unloading branches in order to capture the hysteretic behavior of RC structures.

A very few of these numerical approaches managed to extend their static cyclic models to be implemented for solving dynamic problems. Inoue et al. [17] used the compression field theory for the dynamic analysis of RC shear walls implementing in plain stress elements for wall panels and 8-noded solid elements for slabs supported on wall panels. Cela [18] proposed an elastic-viscoplastic law, based on Drucker-Prager model, subjected to dynamic plain-stress loading conditions, while Kwan et al. [19] suggested an elasticity-based model in order to analyze post-tensioned concrete piers using 8-noded plane stress elements.

Ile and Reynouard [20] combined an elastoplastic isotropic uncracked behavior of concrete energy-based fracture with a smeared crack approach for modeling the cracked concrete with the two-dimensional plane element. Han et al. [21] also proposed a fracture energy-based rotating crack model by using 2D plane elements to analyze a three-storey frame building under a seismic excitation. Mirzabozorg and Ghaemian [22] used a three-dimensional smeared crack approachwith 20-noded isoparametric hexahedral elements, to study concrete gravity dams. In their work, the investigators placed emphasis on the simplicity of the model by using a small number of material parameters.

Other researchers used constitutive models which are based on the principles of continuum damage mechanics. Mazars et al. [23] proposed a lattice model to investigate shear walls under dynamic loads. Faria et al. [24] used 20-noded solid elements and 8-noded plane stress elements to analyze the seismic behavior of an arc dam and a reinforced concrete wall. Richard and Ragueneau [25], proposed the coupling between plasticity and damage modelling. Plasticity is used for the description of concrete in compression, whereas isotropic damage is used for tension. As stated in

their work [25], the pathology of mesh-dependency issues was reduced by adopting a nonlocal approach proposed in [26]. Additionally, Vassaux et al. [27] used a discrete model to define and calibrate quantities such as i) proportional of closed cracks and ii) specific dissipated energy related to friction. These quantities were introduced to the previous model in order to describe the hysteretic behavior of concrete structures obtained by crack closure and friction.

Finally, few researchers conducted 3D dynamic analysis by using 3D constitutive models. Spiliopoulos and Lykidis [28], and Cotsovos [29] used the triaxial constitutive model, introduced by Kotsovos & Pavlovic [2], integrated in 27-noded hexahedral elements. The latter introduce some restrictions with regard to the number of cracks that are allowed to open in each iteration, in an attempt to obtain convergence during the analysis. Moharrami and Koutromanos [30] proposed a 3D constitutive model, which combines the elastoplastic and smeared crack approaches in order to describe the cyclic and dynamic behavior of concrete. It is noteworthy to say here that, none of these researchers investigated the computational efficiency of their proposed models, which is deemed crucial when dealing with full-scale dynamic nonlinear analyses of RC structures.

Most of the studies found in the literature are restricted to 2D analysis in order to capture the biaxial behavior of concrete structures, thus do not provide the numerical tools to study the realistic 3D mechanical behavior of RC structures. In some cases, material models use many numerical restrictions to accomplish stability of their analysis, while other models use complex mathematical procedures in order to describe the nonlinear characteristics of concrete. These customized models are consisted by many material parameters and thus are found to be unable to demonstrate objectivity and numerical robustness for different types of mechanical behaviors and structural geometries. Furthermore, it is evident that a numerical tool, which places emphasis on the simplicity of its formulation and provides numerical robustness and efficiency for the nonlinear cyclic static and dynamic analysis, has to be developed.

The proposed model in this work, describes the triaxial behavior of concrete without the need of introducing a large number of concrete material parameters. The aim of the proposed model is to describe a 3D constitutive material behavior of RC structures with realistic assumptions, which can be easily implemented for any given structural RC member or structure. In this case, only the uniaxial compressive and tensile strengths, the Young Modulus of elasticity and the Poisson's ratio are the material parameters that are required to be defined for the analysis of concrete. The accuracy, numerical simplicity and the computational efficiency are the most important features in order to show the practical use of any model in predicting the nonlinear static and dynamic behavior of RC structures. The proposed model adopts the numerical approach, proposed in [3] (for cyclic loading conditions), thus it is further integrated herein for simulating the dynamic response of RC structures. A new concrete damage factor is presented, which derives from the number of opening/closure cracks, while a second damage factor for steel is also introduced in this work. The numerical RC modelling approach manages to describe the effect of crack closing and crack opening efficiently even for structures which are subjected to a large number of loading cycles. It must be noted here that, the simulation of concrete behavior is based on the proposed model by Markou and Papadrakakis [1] which was an extension of the model presented by Kotsovos and Pavlovic [2]. Additionally, the analytical description of modelling the embedded steel bars within the concrete hexahedral elements can be found in [1, 31]. A thorough numerical investigation has been conducted in order to study the computational efficiency and accuracy of the proposed procedure and presented in sections 3 and 4. The use of rod and beam embedded rebar elements for the simulation of the steel reinforcement was also examined and presented in section 4, where a mesh sensitivity investigation discusses the objectivity of the proposed modeling method.

2. Concrete and steel material constitutive models

A realistic 3D behavior of concrete can be achieved by taking into account in the constitutive material model the out of plane stresses, associated with the triaxial stress-strain phenomena that affect the overall mechanical behavior of the material. In the adopted material model, each state of stress-strain is mathematically described by hydrostatic and deviatoric components, using two moduli of elasticity (bulk K and shear G) and an equivalent external stress (σ_{id}) in order to describe the constitutive relations as presented in [2]. The normal and shear octahedral stresses (σ_0, τ_0) and strains (ε_0, γ_0) are used. The bulk modulus K and the shear modulus G describe the non-linear σ_0-$\varepsilon_{0(h)}$ and τ_0-$\gamma_{0(d)}$ behavior combined with the use of σ_{id} (*id* refers to the hydrostatic component of the internal stress resulting from an external deviatoric stress) in order to take into account the coupling effect of τ_0-$\varepsilon_{0(d)}$ (*h* and *d* refer to the hydrostatic and deviatoric components, respectively). The constitutive relations take the following form:

$$\varepsilon_0 = \varepsilon_{0(h)} + \varepsilon_{0(d)} = (\sigma_0 + \sigma_{id}) / (3K_s) \tag{1}$$

$$\gamma_0 = \gamma_{0(d)} = \tau_0 / (2G_s) \tag{2}$$

where K_s and G_s are the secant forms of bulk and shear moduli, respectively. The secant forms of bulk and shear moduli as well as σ_{id} are expressed as functions of the current state of stress, which is derived by regression analysis of the experimental data as presented in [2].

It is assumed that at the first stages of loading, when the deviatoric stress is less than the 50% of the ultimate strength, the concrete material will practically behave in the elastic region thus the elastic constitutive model of the uncracked material is used [1]. The constitutive material matrix of the uncracked concrete is given by:

$$C = \begin{bmatrix} 2G_t + \mu & \mu & \mu & 0 & 0 & 0 \\ \mu & 2G_t + \mu & \mu & 0 & 0 & 0 \\ \mu & \mu & 2G_t + \mu & 0 & 0 & 0 \\ 0 & 0 & 0 & G_t & 0 & 0 \\ 0 & 0 & 0 & 0 & G_t & 0 \\ 0 & 0 & 0 & 0 & 0 & G_t \end{bmatrix} \tag{3}$$

where $\mu = K_t - 2\ G_t / 3$. When the deviatoric stress exceeds 50% of the ultimate strength, the parameters $K_t=K_t(\sigma_0,\tau_0,f_c)$ and $G_t=G_t(\sigma_0,\tau_0,f_c)$, where f_c represents the uniaxial compressive strength are updated according to the current state of stress in order to account for the concrete material deterioration due to microcracking. .

The concrete's ultimate strength is expressed with the value of the ultimate deviatoric stress by using the expressions of Willam and Warkne [32].

$$\tau_{0u} = \frac{2\tau_{0c}(\tau_{0c}^2 - \tau_{0e}^2)\cos\theta + \tau_{0c}(2\tau_{0e} - \tau_{0c})\sqrt{4(\tau_{0c}^2 - \tau_{0e}^2)\cos^2\theta + 5\tau_{0e}^2 - 4\tau_{0c}^2\tau_{0e}^2}}{4(\tau_{0c}^2 - \tau_{0e}^2)\cos^2\theta + (2\tau_{0e} - \tau_{0c})^2} \tag{4}$$

In Eq.4, the rotational variable θ defines the deviatoric stress orientation on the octahedral plane. The τ_{0e} $(\theta=0°)$ and τ_{0c} $(\theta=60°)$ correspond to the ultimate limit states of $\sigma_1=\sigma_2>\sigma_3$ (triaxial extension) and $\sigma_1>\sigma_2=\sigma_3$ (triaxial compression), respectively, that are taken from experimental data. The numerical model is based on the brittle nature of concrete, therefore, when the criterion of failure is satisfied the material point loses its capacity abruptly. The model is combined with the smeared crack approach that treats cracking by redistributing the released stresses to the surrounding uncracked concrete.

The constitutive matrix of a cracked concrete element is modified by setting to zero the stiffness that corresponds to the direction of the maximum principle tensile stress. Similarly, the constitutive matrix is updated in the case of two cracks, by assuming a remaining stiffness along the intersection of the two planes of cracks only [1]. The stresses are calculated through the use of the following expression:

$$\sigma_{Cr} = \mathbf{T^{-1}}\left[\sigma_1 = 0 \quad \sigma_2 \quad \sigma_3 \quad 0 \quad 0 \quad 0\right]^T \tag{5}$$

where T^{-1} is the inverse transformation matrix that is used to transform the principal stress axes to the initial x, y and z axes.

Furthermore, the use of a modified crack-closure criterion is used herein, which is crucial for the stability of the nonlinear analysis procedure when dealing with cyclic loading conditions. The criterion, introduced in [5], uses the strains associated with the initial formation of the cracks in order to determine whether a closing crack will be eventually closed during the numerical procedure. The criterion of closing crack takes the following form:

$$\varepsilon_i \leq a \cdot \varepsilon_{cr} \tag{6}$$

where ε_i is the current strain in the i-direction which is normal to the crack plane and ε_{cr} is the strain that caused the crack formation. Parameter *a* is a reduction factor, which takes the following form:

$$a = 1 - \frac{\varepsilon_{cr}}{\varepsilon_{\max}} = \frac{\varepsilon_{\max} - \varepsilon_{cr}}{\varepsilon_{\max}} \tag{7}$$

The maximum strain ε_{max} is determined through the nonlinear Newton-Raphson procedure, whereas, in every internal Newton-Raphson iteration, the strains are calculated along the norm of the crack planes. Therefore, during an internal iteration, when a crack is formed at a Gauss point, it is assumed that $\varepsilon_{max} = \varepsilon_{cr}$. Then, for every Newton-Raphson *i* iteration the strains ε_i normal to the crack planes are checked if they are larger than the previously calculated ε_{max}. If this is the case, then ε_{max} is set equal to ε_i. More details regarding the closing crack criterion can be found in [3], where it is assumed that the elastic constitutive matrix is used to calculate the stresses of the previously cracked Gauss point. In this work, an improvement is proposed concerning the formulation of the constitutive matrix of the previously cracked Gauss point, by introducing a damage factor. For the case of the steel material model, a damage factor is also adopted in conjunction with the Menegotto-Pinto material model, which will be discussed in section 2.2.

2.1 Damage factor D_c for concrete

During strong earthquake motions, RC structures develop excessive nonlinear behavior that is caused mainly by the intense cracking of concrete, where the steel reinforcement can also yield or rapture. The number of cracks that open is an indication of the magnitude of damage that has occurred at each RC member. Generally, the material deterioration caused by the opening and closing of cracks can determine the hysteretic behavior of the structure.

Many researchers tried to simulate the hysteretic behavior of RC structures by using damping mechanisms. The damping behavior of RC structures is still an open subject of research. Most of the studies assume a constant viscous damping with high values of damping ratios throughout the nonlinear analysis, by using the Rayleigh or a proportional damping model. In this case, the hysteretic curves, which are obtained from the numerical analysis, are characterized as constant ellipses, where the mechanical behavior of the structure is attributed to the viscosity mechanisms that are activated during the nonlinear dynamic response.

However, the experimentally derived hysteretic loops are usually characterized by more abrupt changes in terms of stiffness while the corresponding P-δ curves present significant pinching effects. A numerical simulation of damping effect based on the hysteretic behavior of the structure could result in a more rigorous formulation in capturing the dynamic response and the complicated physical phenomena that occur due to the opening and closing of cracks. In this article, the concrete material deterioration is integrated with a new damage factor that is directly connected to the phenomenon of opening and closing of cracks in order to better describe the hysteretic behavior of RC structures and capture the pitching effect.

The material deterioration factor has to take into account the level of cracking (damage), the number of times that a crack has been closed and generally, to be associated with the dissipated energy that occurs due to the nonlinear structural behavior. The parameter *a* in Eq. 7, which is used in the crack closing criterion [5], is an expression of the strains that were developed at a cracked Gauss point after the crack opening. It is therefore a quantity that expresses the level of energy that is consumed at a cracked Gauss point. When the parameter *a* increases, the consumed energy increases and the damage of the structural member becomes more pronounced due to the material deterioration. Moreover, the expression -(1-*a*) is proportional to the damage that occurs at a cracked Gauss point (this expression is suitable when used within an exponential function that outputs values lower than 1, considering that $0 \leq a \leq 1$). When a crack opens and closes, material damage is accumulated because of the developed irreversible strains at that specific area. It is obvious that the more times the cracks are closing and opening at a certain area, this area loses the ability to retrieve the uncracked stiffness. Based on this mechanism, the expression of the damage factor that is proposed in this work takes the following form:

$$D_c = e^{-(1-a)/f_{cc}} = e^{-\left(1-\left(1-\frac{\varepsilon_{cr}}{\varepsilon_{\max}}\right)\right)/f_{cc}} = e^{-\left(\frac{\varepsilon_{cr}}{\varepsilon_{\max}}\right)/f_{cc}} \tag{8}$$

where f_{cc} is the number of times that a crack has closed, which is updated at every Newton-Raphson iteration for each Gauss point. A schematic representation of Eq. 8 can be seen in the Fig. 1.

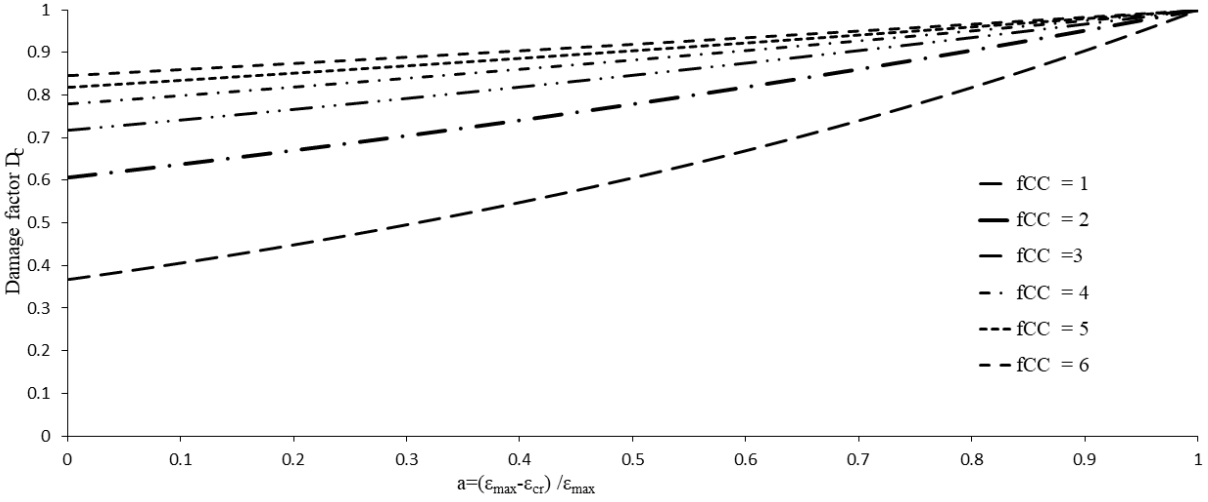

Fig. 1. Schematic representation of the values of the damage factor D_c as a function of the parameter *a* and f_{CC}

When the criterion of crack-closure (Eq. 6) at a Gauss point is satisfied, (assuming that this Gauss point had prior to that only one crack formation), a part of the stiffness is lost (according to Fig. 1) along the previous crack plane which was assumed to form in an orthogonal direction to the maximum principle tensile stress. Therefore, the stiffness degradation is directly connected to the number of times a crack has opened and closed, thus accumulating the energy loss due to this

phenomenon. By assuming that the crack is formed perpendicular to the x' axis and by using Eq. 3, the constitutive matrix takes the following form:

$$C_l^{'} = \begin{bmatrix} a_n \cdot (1-D_c) \cdot (2G_t + \mu) & a_n \cdot (1-D_c) \cdot \mu & a_n \cdot (1-D_c) \cdot \mu & 0 & 0 & 0 \\ a_n \cdot (1-D_c) \cdot \mu & 2G_t + \mu & \mu & 0 & 0 & 0 \\ a_n \cdot (1-D_c) \cdot \mu & \mu & 2G_t + \mu & 0 & 0 & 0 \\ 0 & 0 & 0 & a_s \cdot (1-D_c) \cdot \beta \cdot G_t & 0 & 0 \\ 0 & 0 & 0 & 0 & a_s \cdot (1-D_c) \cdot \beta \cdot G_t & 0 \\ 0 & 0 & 0 & 0 & 0 & a_s \cdot (1-D_c) \cdot \beta \cdot G_t \end{bmatrix} \quad (9)$$

where β is a shear retention factor and, a_n and a_s are constants with recommended values of 0.25 and 0.125, respectively. The parameters a_n and a_s were defined following a parametric investigation conducted through the use of a number of RC structural members subjected to cyclic loading conditions, which will be presented in section 2.3. Similarly, in the case when two cracks are closing and assuming that the cracks were perpendicular to the x' and y' axes the constitutive matrix takes the following form:

$$C_l^{''} = \begin{bmatrix} a_n \cdot (1-D_c) \cdot (2G_t + \mu) & a_n \cdot (1-D_c) \cdot \mu & a_n \cdot (1-D_c) \cdot \mu & 0 & 0 & 0 \\ a_n \cdot (1-D_c) \cdot \mu & a_n \cdot (1-D_c) \cdot (2G_t + \mu) & a_n \cdot (1-D_c) \cdot \mu & 0 & 0 & 0 \\ a_n \cdot (1-D_c) \cdot \mu & a_n \cdot (1-D_c) \cdot \mu & 2G_t + \mu & 0 & 0 & 0 \\ 0 & 0 & 0 & a_s \cdot (1-D_c) \cdot \beta \cdot G_t & 0 & 0 \\ 0 & 0 & 0 & 0 & a_s \cdot (1-D_c) \cdot \beta \cdot G_t & 0 \\ 0 & 0 & 0 & 0 & 0 & a_s \cdot (1-D_c) \cdot \beta \cdot G_t \end{bmatrix} \quad (10)$$

The proposed expressions of the constitutive matrix (Eqs. 9 and 10) describes the anisotropic behavior of concrete at the local coordinate system, therefore, it has to be transformed to the global system by using the standard coordinate system transformation laws as follows:

$$C_g = T^T C_l T \quad (11)$$

where T is the transformation matrix given in Eq. 12 with the direction cosines given by (l_i, m_i, n_i), which define the relative orientation of the i-axis of the system (x´, y´, z´) to (x, y, z), respectively.

$$T = \begin{bmatrix} l_1^2 & m_1^2 & n_1^2 & l_1 m_1 & m_1 n_1 & n_1 l_1 \\ l_2^2 & m_2^2 & n_2^2 & l_2 m_2 & m_2 n_2 & n_2 l_2 \\ l_3^2 & m_3^2 & n_3^2 & l_3 m_3 & m_3 n_3 & n_3 l_3 \\ 2l_1 l_2 & 2m_1 m_2 & 2n_1 n_2 & l_1 m_2 + l_2 m_1 & m_1 n_2 + m_2 n_1 & n_1 l_2 + n_2 l_1 \\ 2l_3 l_1 & 2m_3 m_1 & 2n_3 n_1 & l_3 m_1 + l_1 m_3 & m_3 n_1 + m_1 n_3 & n_3 l_1 + n_1 l_3 \\ 2l_2 l_3 & 2m_2 m_3 & 2n_2 n_3 & l_2 m_3 + l_3 m_2 & m_2 n_3 + m_3 n_2 & n_2 l_3 + n_3 l_2 \end{bmatrix} \quad (12)$$

It must be noted here that, the constitutive matrix correspond to the cases when a crack is closed at a Gauss point, which had previously one, two or three cracks. After the crack closure, the stresses are corrected by using the following expression:

$$\sigma^i = \sigma^{i-1} + C_g \cdot \Delta\varepsilon^i \quad (13)$$

Finally, when all cracks at a Gauss point have been closed (uncracked Gauss point) and the reduction factor of one of the previous cracks is larger than 0.5, then the constitutive matrix takes the following form:

$$C_g{}' = (1-D_c) \cdot C_g \quad (14)$$

It was found via a numerical investigation that when the reduction factor of one of the previous cracks is larger than 0.5, then the accumulated damage is severe and Eq. 14 has to be implemented

in order to take this phenomenon into account when the Gauss point is considered uncracked. The proposed algorithms for treating cracked and uncracked Gauss points are described in the flow charts presented in Figs. 2, 3 and 4. The flow charts present the algorithm that is used in order to update the stresses of the previous (i-1) Newton-Raphson internal iteration to the current one (i).

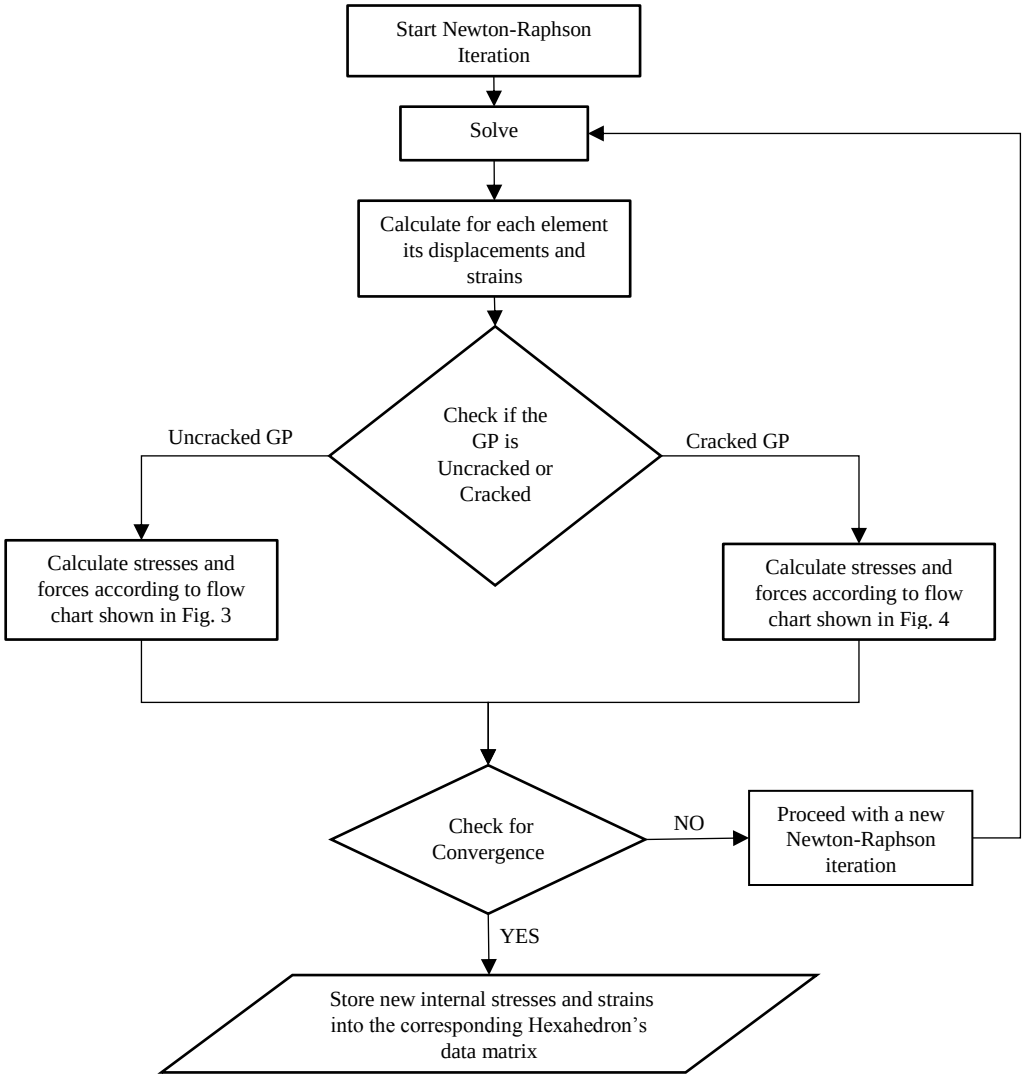

Fig. 2. Flow chart of the proposed algorithm of the concrete material model.

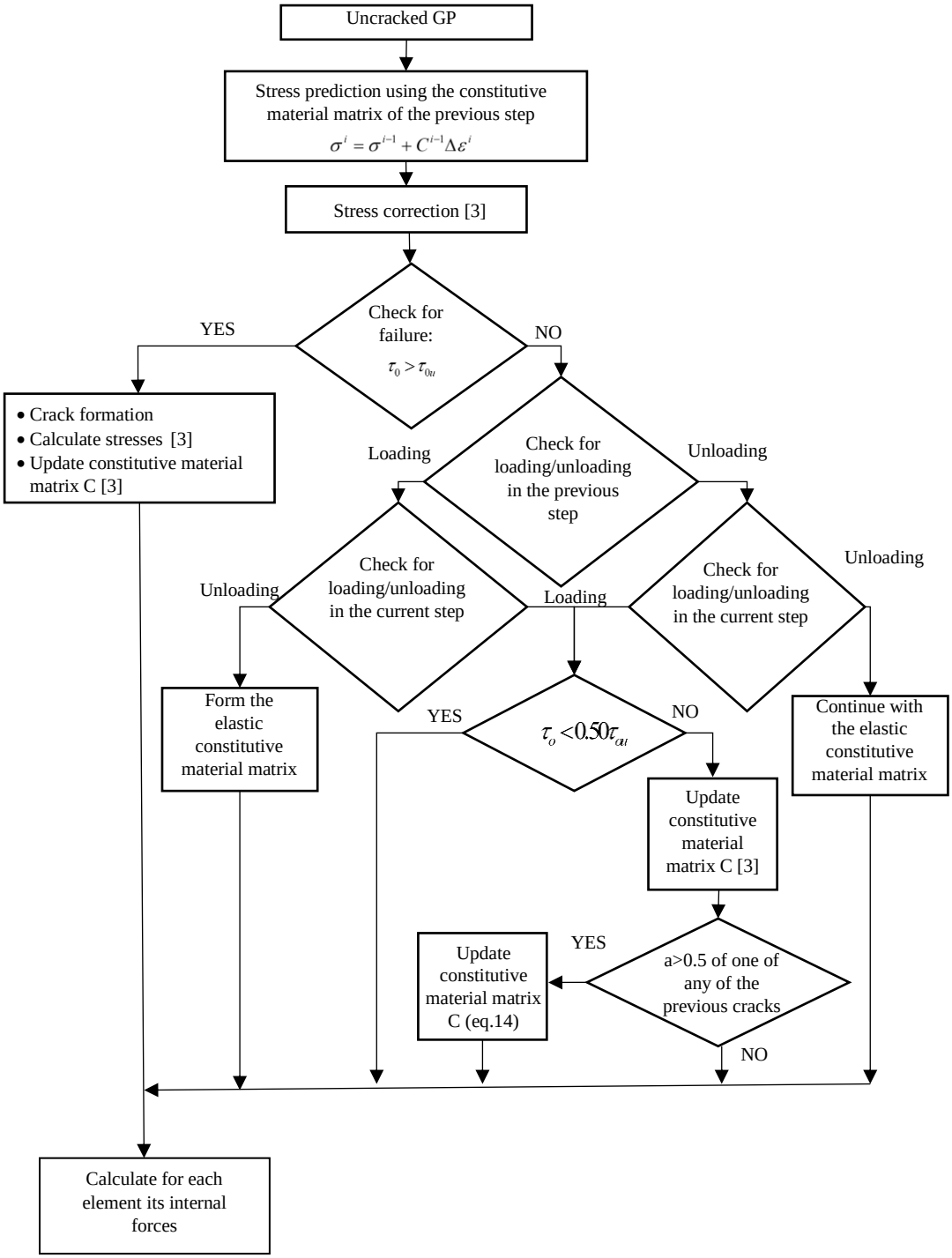

Fig. 3. Flow chart of the proposed algorithm for updating the stress-strain tensors and constitutive matrix for the case of an uncracked Gauss point.

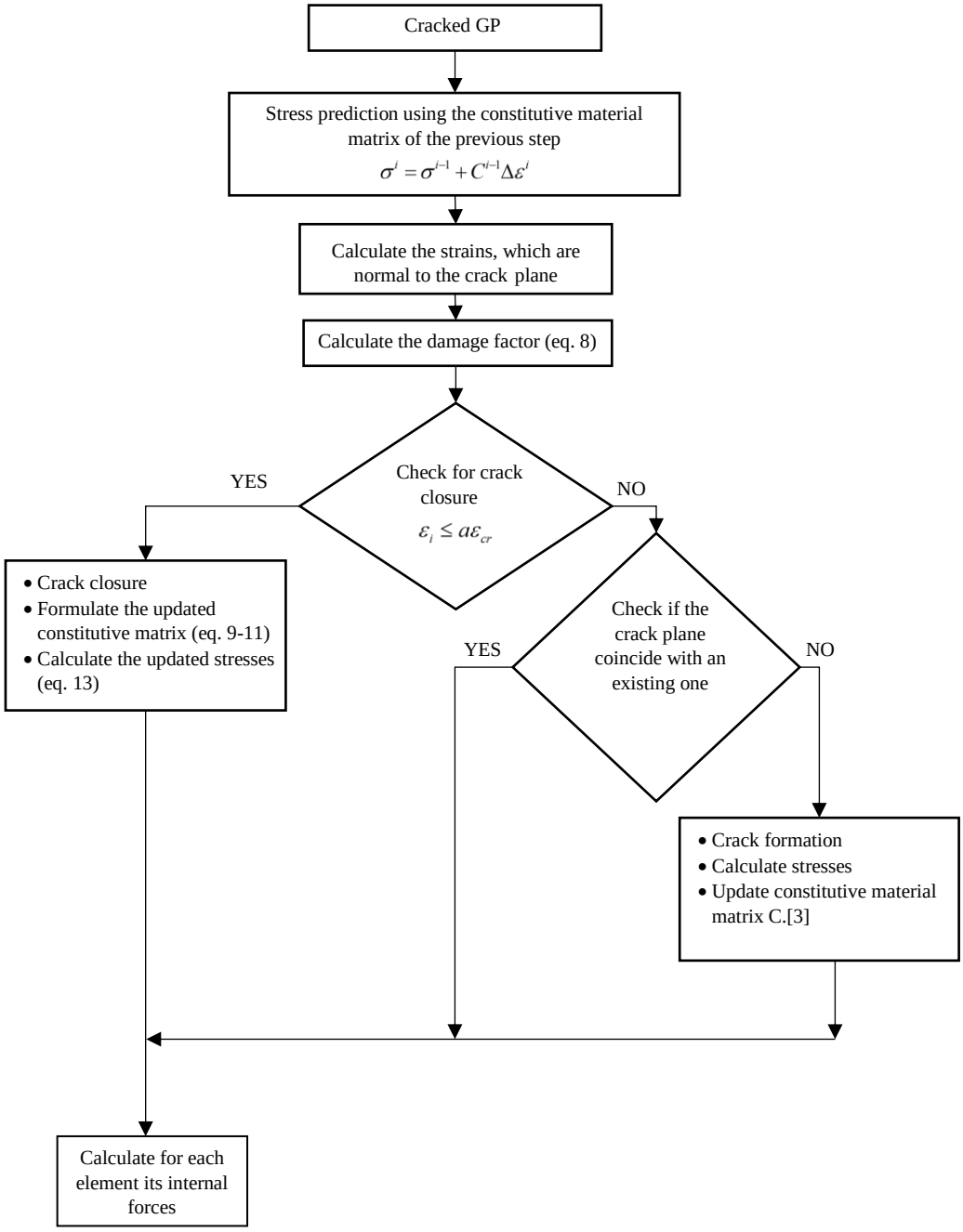

Fig. 4. Flow chart of the proposed algorithm for updating the stress-strain tensors and constitutive matrix for the case of a cracked Gauss point.

2.2 Damage factor D_s for steel reinforcement

The steel reinforcement is modelled through the use of the Menegotto-Pinto [33] model that takes into account the Bauchinger effect. In shear dominated areas of a RC structure, the severe inclined cracking leads to significant strength deterioration of steel reinforcement thus affecting hysteretic loops of the entire RC member. Experimental results show that RC structures with significant shear deformations develop severe pinching characteristics around zero load. In these shear dominated areas, the steel reinforcement also develops shear deformations and debonding effects from concrete. The re-opening and re-closing of cracks at low level of shear forces enhance the slipping phenomena and leads to significant stiffness and strength deterioration of the structure. The influence of opening and closing cracks to the pinching phenomenon is described experimentally in [34, 35]. The influence of the pinching effect may be modelled by a modification of the steel stress-strain relation as described in [36]. Thus, the pinching phenomenon can indirectly

be taken into account using a reduced stiffness contribution of the steel reinforcement by defining the accumulated damage due to the crack opening/closure effect. This reduction can also be characterized as the loss of bonding between steel reinforcement with the surrounding damaged concrete.

The level of damage that occurs due to the opening of cracks can be expressed with Eqs. 7-10. The average value of all parameters *a* (Eq. 7), at the 8 Gauss points within a single hexahedral finite element, can determine the level of damage within the volume of the hexahedral element which can be expressed by the following expression:

$$D_s = \left[1 - a_{Element}\right] \tag{15}$$

where,

$$a_{Element} = \frac{\sum_{1}^{ncr} a_i}{ncr} \text{ and } ncr \text{ is the number of cracked Gauss points} \tag{16}$$

In the case of unloading, when the structure reaches zero deformation, a material deterioration of the steel reinforcement is estimated according to the following expression:

$$E_s^{'} = (1 - D_s) E_s \tag{17}$$

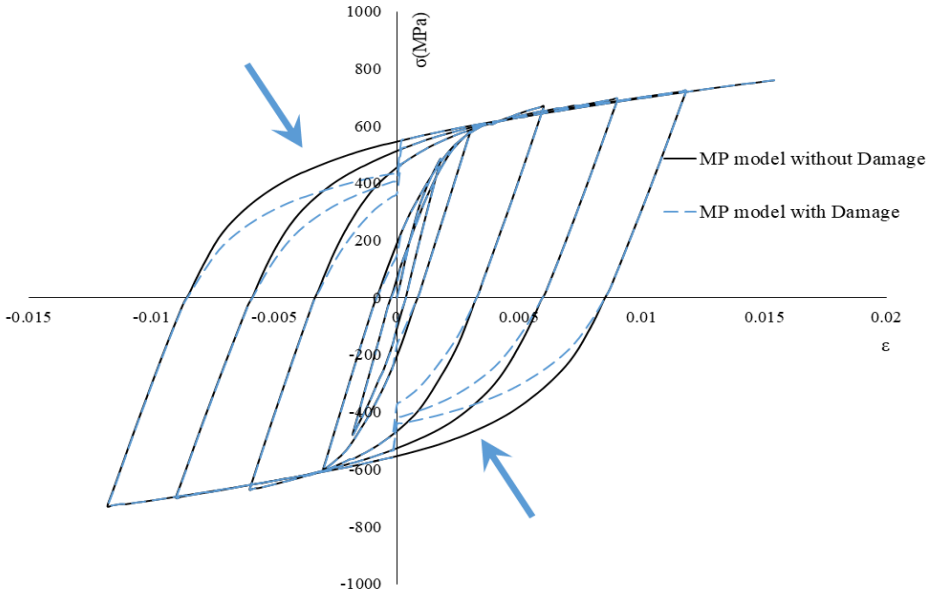

Fig. 5. Menegotto-Pinto steel model that accounts for the accumulated damage due to the opening and closure of cracks.

The material deterioration is applied when $\sigma_s \cdot \varepsilon_s < 0$, which describes the situations when crack closures and re-openings occur and the pinching phenomena are excessive. The σ-ε curves of the Menegotto-Pinto material model that uses the proposed steel damage factor is shown in Fig. 5.

According to [13, 37], the pinching phenomenon, which leads to the reduction of the energy dissipation capacity, is eliminated by the proper orientation of steel grid that is aligned to the direction of the applied principal stresses. Therefore, it is difficult to always explain the causes of the appearance of these pinching characteristics. The proposed modification of the steel Menegotto-Pinto model is a direct way to capture this phenomenon by taking into account the level of cracking that occurred in the surrounding area of the steel rebar, which in our case is the hexahedral element that hosts the embedded rebar. The proposed damage factors D_c and D_s are investigated in section 3, while the parametric investigation for defining the values of the parameters a_n and a_s is presented in the following section.

2.3 Parametric investigation for defining constants a_n and a_s

The Del Toro Rivera [38] interior frame joint of Fig. 6a, which was analyzed in [3], is used to investigate and define the optimum values of the constant parameters a_n and a_s. The numerical results obtained for this model in [3] are defined herein as the results obtained by the "initial model" that does not use the proposed damage factors. The structural member was subjected to different cyclic loading conditions according to the experimental test. The geometry and reinforcement details are illustrated in Fig. 6a. The concrete domain was discretized with 8-noded hexahedral finite elements and the steel reinforcement was discretized with beam elements (Fig. 6b). In order to avoid inducing parasitic stiffness within the numerical model when the cracking will occur, the values of the parameters a_n and a_s have to be lower than 1 to account for the stiffness reduction due to the material deterioration. Numerous combinations of the values of a_n and a_s have been tested, where the results of the five combinations that were found to better capture the experimental data are shown in Table 1.

Table 1. Combinations of the values a_n and a_s that were investigated.

Combination	a_n	a_s
1	0.25	0.125
2	0.5	0.5
3	0.5	0.125
4	1	1
5	0.125	0.125

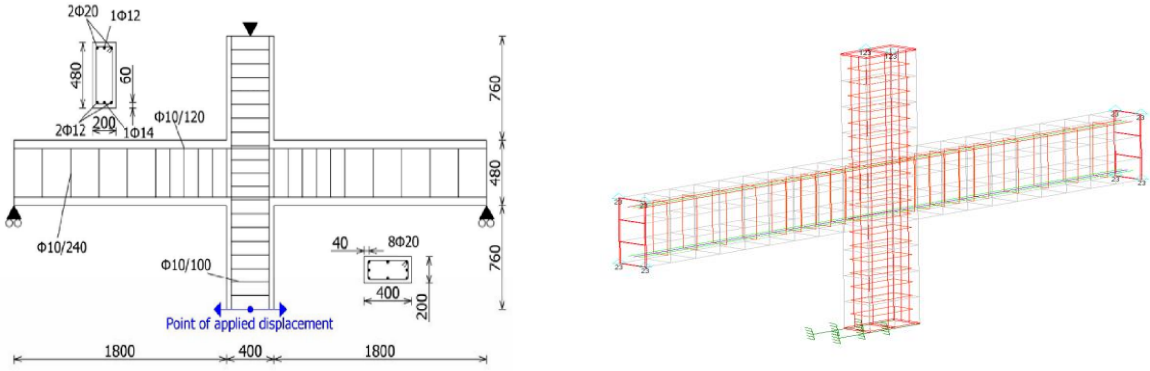

(a) (b)

Fig. 6. Interior frame joint. (a) Geometry and reinforcement details of the beam-column joint [38] and (b) 3D view of the FE mesh of concrete elements and steel reinforcement. [3]

The computed curves are given in Fig. 7, where it can be seen that the numerically obtained results match very well the experimental data. It was also found that the values of a_n and a_s have influenced the dissipated energy that derived from the hysteretic curves. Tables 2, 3 and 4 show the values of the dissipated energy (as the area of every hysteretic curve) that were obtained by using different set of parameter values (a_n, a_s). It can be seen that the numerical curves with the smallest divergence were obtained when using the set of values of $a_n = 0.25$ and $a_s = 0.125$.

Furthermore, the load carrying capacity of the specimen was accurately predicted by all the numerical curves (divergences $\leq 15\%$). Table 5 shows the comparison of the initial model and the proposed model with the experimental data in terms of maximum horizontal load for each loading cycle.

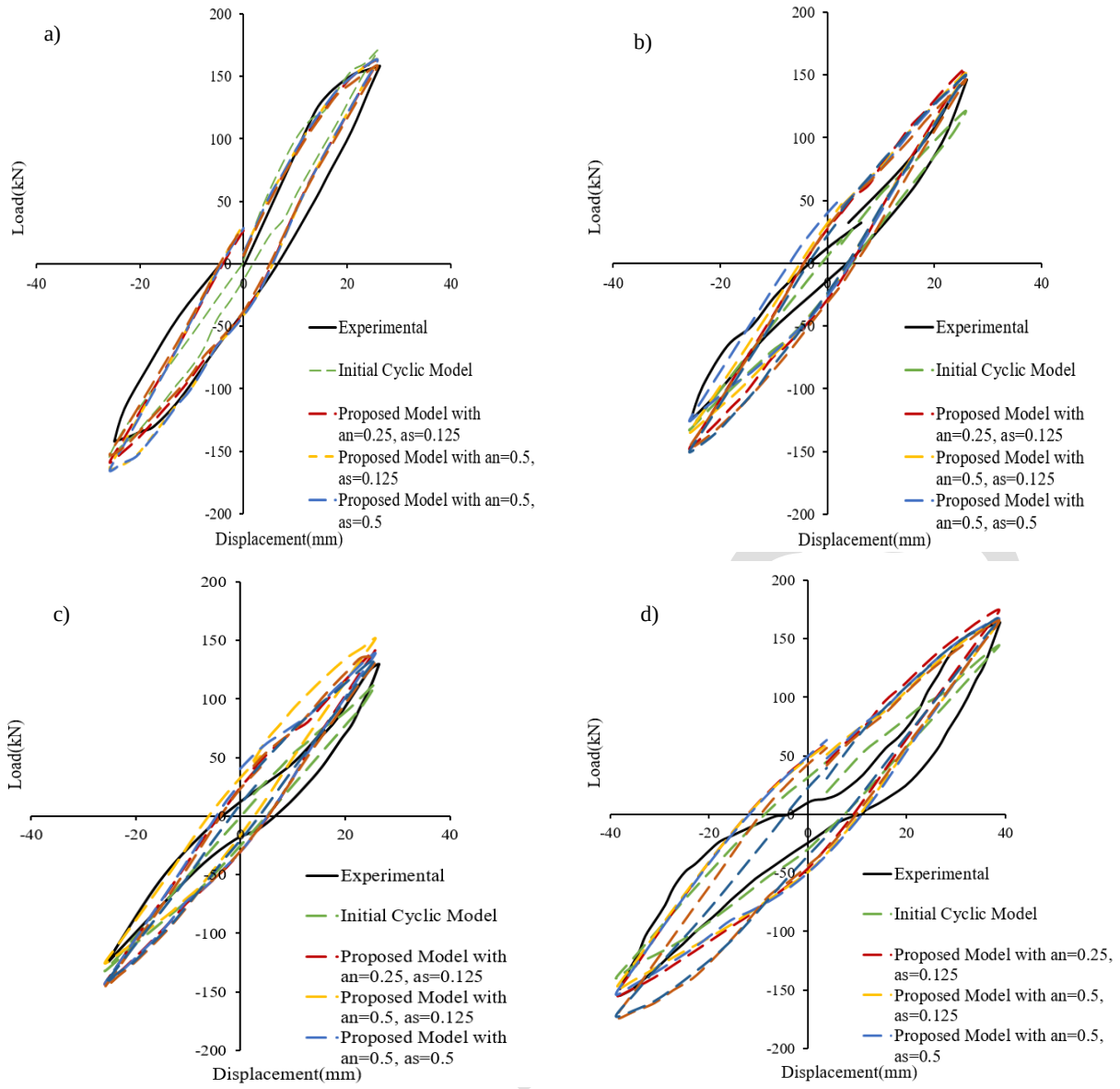

Fig. 7. Interior frame joint. Comparison between numerical and experimental results with different values of a_n and a_s for the cases of a) first cycle b) second cycle, c) third cycle and d) forth cycle.

Table 2. Comparison of the dissipated energy between experimental results and the proposed numerical model.

Interior Frame Joint	Dissipated Energy Experimental (kN mm)	Dissipated Energy Initial Model (kN mm)	Divergence from experimental (%)	Dissipated Energy Proposed Model a_n=0.25,a_s=0.125 (kN mm)	Divergence from experimental (%)
1st Cycle	2596.34	1165.14	55.12	1933.84	25.52
2nd Cycle	1264.12	669.37	47.05	1560.56	23.45
3rd Cycle	1212.48	942.65	22.25	1570.65	29.54
4th Cycle	3287.87	1953.10	40.60	4335.26	31.86
		Average	41.26	Average	27.59

Table 3. Comparison of the dissipated energy between experimental results and the numerical model with an = 0.5 and as = 0.5, 0.125.

Interior Frame Joint	Dissipated Energy Experimental (kN mm)	Dissipated Energy Proposed Model a_n=0.5, a_s=0.5 (kN mm)	Divergence from experimental (%)	Dissipated Energy Proposed Model a_n=0.5, a_s=0.125 (kN mm)	Divergence from experimental (%)
1st Cycle	2596.34	2150.51	17.17	2187.91	15.73
2nd Cycle	1264.12	1843.40	45.82	1598.99	26.49

3rd Cycle	1212.48	1727.10	42.44	1727.10	42.44
4th Cycle	3287.87	4450.10	35.35	4365.63	32.78
		Average	35.20	Average	29.36

Table 4. Comparison of the dissipated energy between experimental results and the numerical model with an = 0.125, 1 and as = 0.125, 1.

Interior Frame Joint	Dissipated Energy Experimental (kN mm)	Dissipated Energy Predicted Proposed a_n=1, a_s=1 (kN mm)	Divergence from experimental (%)	Dissipated Energy Predicted Proposed a_n=0.125, a_s=0.125 (kN mm)	Divergence from experimental (%)
1st Cycle	2596.34	2168.55	16.48	1928.35	25.73
2nd Cycle	1264.12	1771.44	40.13	1793.78	41.90
3rd Cycle	1212.48	1820.81	50.17	1721.63	41.99
4th Cycle	3287.87	4197.97	27.68	4039.17	22.85
		Average	33.62	Average	33.12

Table 5. Comparison of the horizontal load of each cycle between experimental and numerical results of the initial and the proposed model.

Interior Frame Joint	Horizontal Load Experimental (kN)		Horizontal load Predicted Initial (kN)		Divergence from Experimental		Horizontal load Predicted Proposed (kN)		Divergence from Experimental	
	Positive	Negative	Positive	Negative	Positive (%)	Negative (%)	Positive	Negative	Positive (%)	Negative (%)
1st Cycle	158	-142	177	-165	12.03	16.20	162	-159	2.58	11.83
2nd Cycle	146	-126	125	-146	14.38	15.87	156	-148	6.66	17.63
3rd Cycle	130	-124	118	-139	9.23	12.10	142	-144	9.49	15.82
4th Cycle	164	-154	144	-178	12.20	15.58	175	-155	6.59	0.65
				Avg.	11.96	14.94		Avg.	6.33	11.48

3. Numerical Validation of the Proposed Model for Static Cyclic Analysis

In this section, the numerical validation of the proposed model will be presented for the case of static cyclic analysis under ultimate loading conditions. It must be noted at this point that all the numerical tests presented in this research work have been performed by using a computer with a processing power of 2.50 GHz.

3.1 RC Beam-Column Joint

The beam-column joint shown in Fig. 8, was tested by Shiohara and Kusuhara [39] under static cyclic loading. The uniaxial compressive concrete strength was reported to be equal to f_c = 28.3 MPa and the yielding stress of the steel reinforcement was 456 MPa for the 13 mm diameter bars in the beam section, while the yielding stress of the bars, placed within the column section, was 357 MPa. The Young modulus of elasticity for the longitudinal bar reinforcement was reported to be equal to E_S = 176 GPa. For the stirrup reinforcement, 6 mm in diameter rebars were used with a yielding stress of 326 MPa and a Young modulus of elasticity equal to 151 GPa.

The frame joint was subjected to different cyclic loading sets according to the according experiment. The loading history that was numerically applied in this work, is presented in the form of 15 cycles of imposed displacements in Fig. 9. The concrete domain was discretized with 8-noded hexahedral finite elements and the steel reinforcement was discretized with beam elements. A total number of 128 concrete (23cm x 15cm x 15cm) and 888 steel elements were used to discretize the entire frame joint, as illustrated in Fig. 9.

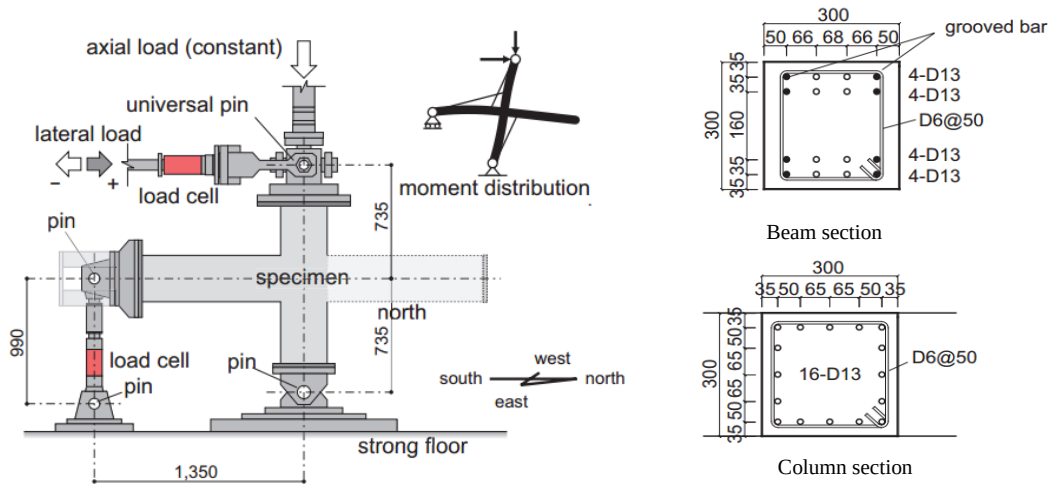

Fig. 8. Geometry and reinforcement details of the beam-column joint [39]. All dimensions are in mm.

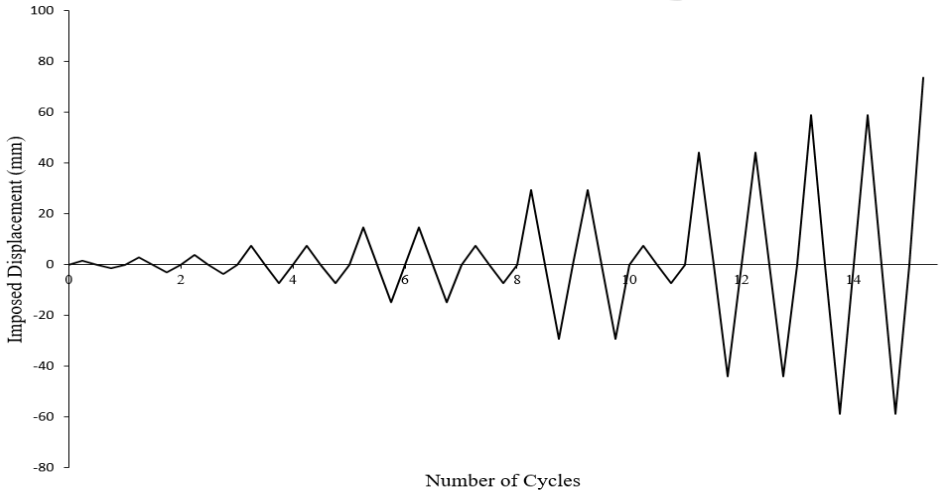

Fig. 9. Imposed displacement history of the interior frame joint.

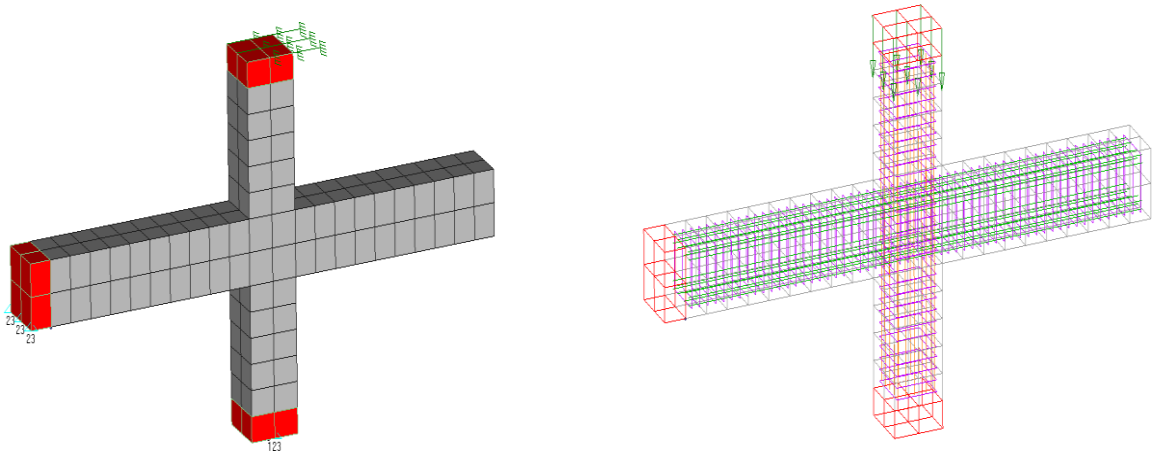

(a) (b)

Fig. 10. RC beam-column frame joint. (a) FE concrete mesh with imposed displacements, (b) steel reinforcement elements and applied loads.

The boundary conditions of the numerical model can be seen in Fig. 10, where the displacements were imposed at the top section of the column, while a 216 kN compressive force was also applied at the same section. Additionally, 8-noded hexahedral finite elements were used at the support and at the top sections of the column (red color, where the displacements are imposed) in order to simulate the metallic plates, which were placed in order to avoid local failure.

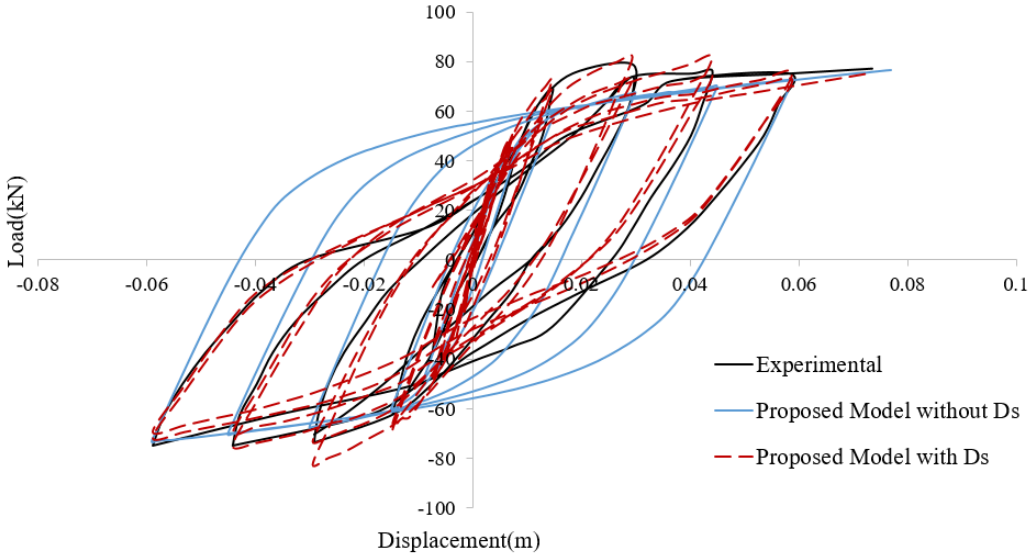

Fig. 11. Beam-Column frame joint. Comparison between numerical and experimental results. Complete force-displacement history.

The computed force-displacement curves are compared with the corresponding experimental data in Fig. 11. As can be seen, the numerical results match very well with the experimental data, where the stiffness and the resulted load-carrying capacity of the specimen were predicted in an accurate manner. Furthermore, the numerical energy dissipation values are very close to the experimental ones. Fig. 11 also shows the force-displacement curve when the proposed modification for the Menegotto-Pinto model is not applied (the D_S damage factor is set to 0). Furthermore, the numerical results show that the proposed modification manages to capture the pinching effect in the case where both proposed damage factors were activated. During the analysis, the steel rebars did not develop severe yielding but a bond degradation has occurred due to the opening of diagonal cracks inside the joint, according to the experimental results reported in [39]. This observation indicates the importance of accounting the damage within the concrete domain and numerically transferring it to the steel rebars through the proposed damage factor D_S. Additionally, Tables 6 and 7 show the comparison of the numerical and experimental results in terms of dissipating energy and load carrying capacity for cycles 5, 7, 9, 10, 13 and 15, which correspond to the last cycle of each imposed displacement (see Fig. 9) . The experimental data show that in the first three cycles the structural member is in the elastic region and show negligible dissipating energy, which comply with the numerical findings. Table 6, shows that the numerical curves capture the corresponding experimental ones in terms of dissipating energy by an average value of 20%. Furthermore, Table 7 shows that the load carrying capacity of the structural member was accurately predicted deriving an average error value lower than 10%. Finally, according to [39], the first rebar yielding within the beam was observed when the shear of the structure was 63.3 kN. The first yielding of beam rebars during the numerical model analysis occurred when the shear of the structure was 65.91 kN (which represents a 4% deviation from the experimentally observed magnitude).

Table 6. Comparison of the dissipated energy between the experimental and numerical data.

RC Joint	Dissipated Energy Experimental (kN mm)	Dissipated Energy Predicted (kN mm)	Divergence from Experimental (%)
5^{th} Cycle	195.23	105.46	45.98
7^{th} Cycle	460.85	564.24	22.43
9^{th} Cycle	2662.45	2540.25	4.59

10th Cycle	1791.00	2310.61	29.01
13st Cycle	4719.40	4275.83	9.40
15th Cycle	6174.95	5372.14	13.00
		Average	20.74

Table 7. Comparison of the horizontal load of each cycle between experimental and numerical results of the proposed model.

RC Joint	Horizontal load Experimental (kN)		Horizontal load Predicted Proposed (kN)		Divergence from Experimental	
	Positive	Negative	Positive	Negative	Positive (%)	Negative (%)
5th Cycle	43.75	-37.5	50.45	-47.22	15.31	-25.93
7th Cycle	69.38	-62.5	68.78	-65.91	0.86	-5.45
9th Cycle	78.75	-73.75	81.62	-82.49	3.64	-11.85
10th Cycle	73.75	-70.454545	72.85	-73.17	1.23	-3.85
13st Cycle	76.14	-75	74.05	-69.84	2.74	-6.89
15th Cycle	75.00	-75	72.15	-69.19	3.80	-7.75
				Average	4.60	-10.29

Overall, the proposed modeling approach managed to capture the cyclic mechanical behavior for all imposed displacement cycles with an acceptable accuracy.

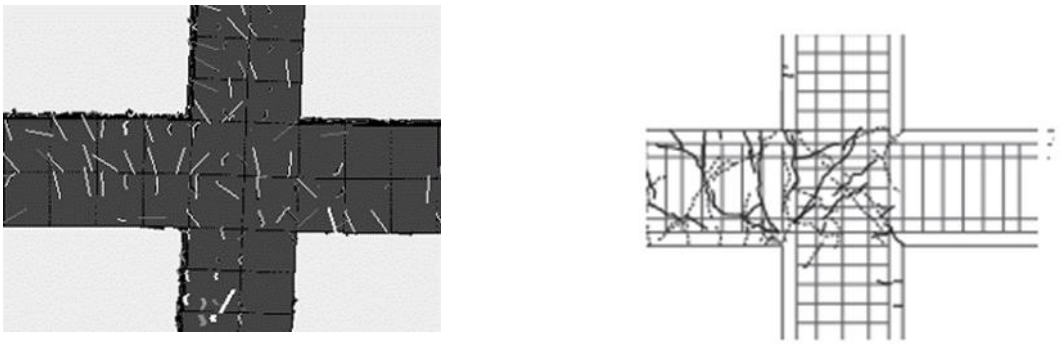

Fig. 12. RC beam-column frame joint. Comparison of experimentally and numerically obtained crack patterns.

The crack patterns near the failure mode is depicted in Fig. 12, where it can be observed that the cracks within the joint indicate a characteristic shear diagonal cracking pattern. The numerical model appears to be more heavily cracked than the experimental one, which is attributed to the assumption of the smeared crack approach. Nonetheless, the crack pattern shows that the crack formation is numerically captured in a realistic manner in-terms of location and direction.

The required Newton-Raphson internal iterations per displacement increment are shown in Fig. 13, where an energy convergence tolerance criterion with the acceptable numerical error of 10^{-4} is adopted. It can be seen that, all displacement increments in Fig. 13 required a reasonable number of internal iterations to reach convergence regardless the intense nonlinear behavior of the structure. Thus, 77% of the displacement increments require less than 5 internal iterations to converge, while 95% of the displacement increments require less than 10 internal iterations. The computational time for the nonlinear solution procedure, as given in Table 8, is 173 seconds to perform 610 displacement increments, which illustrates the overall stability of the proposed nonlinear solution procedure that allows for a complete analysis in less than 3 minutes.

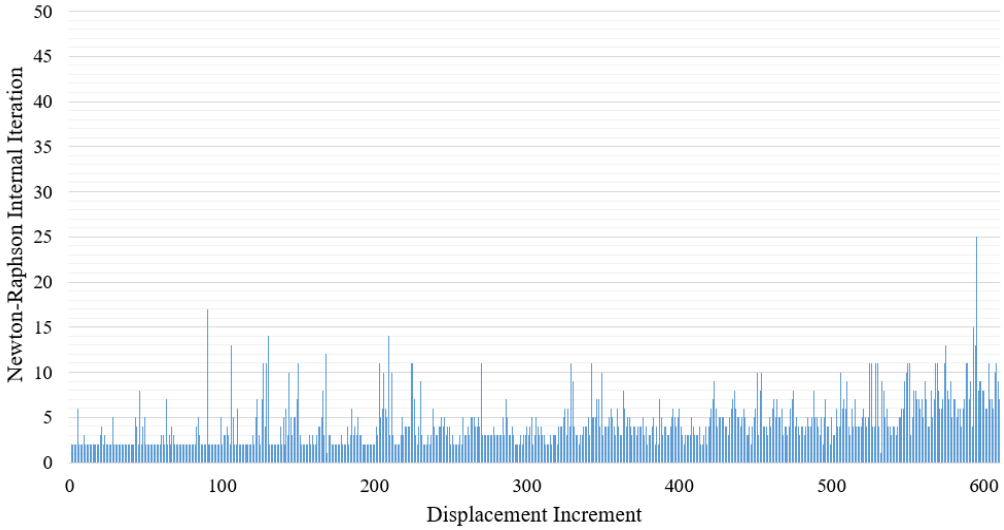

Fig. 13. RC beam-column frame joint. Required Newton-Raphson iteration per displacement increment.

Table 8. RC beam-column frame joint. CPU time for different tasks of the numerical solution.

Task	CPU Time (s)
Embedded rebar element mesh generation	0.1
Nonlinear incremental-iterative solution	173
Total Time	173.1

3.2 RC Column

The second structural member, which was numerically investigated with the proposed model, is a RC column that was subjected to ultimate limit state cyclic loading conditions. This column was experimentally investigated by Saatcioglou and Ozcebe [40]. The uniaxial compressive concrete strength was reported to be equal to f_c = 32 MPa and the yielding stress of the steel reinforcement was 438 MPa for the 25 mm rebars used to reinforce the beam section, while the yielding stress for the 10 mm rebars found in the column section was 470 MPa. The geometry, reinforcement details and the mesh of the finite element model are illustrated in Fig. 14.

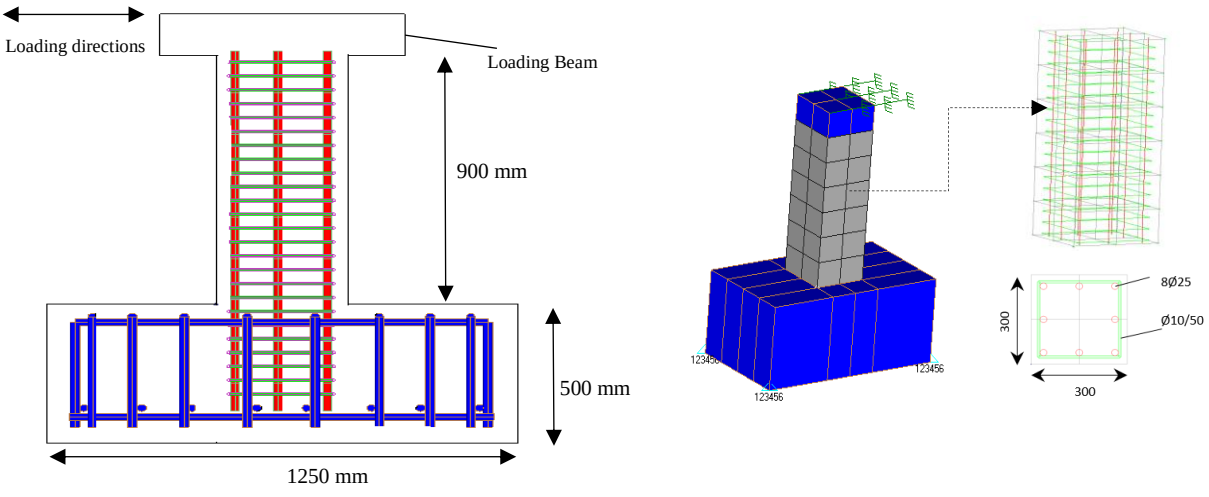

(a) (b)

Fig. 14. RC Column. (a) Geometry and reinforcement details [40] (b) Hexahedral and embedded rebar meshes.

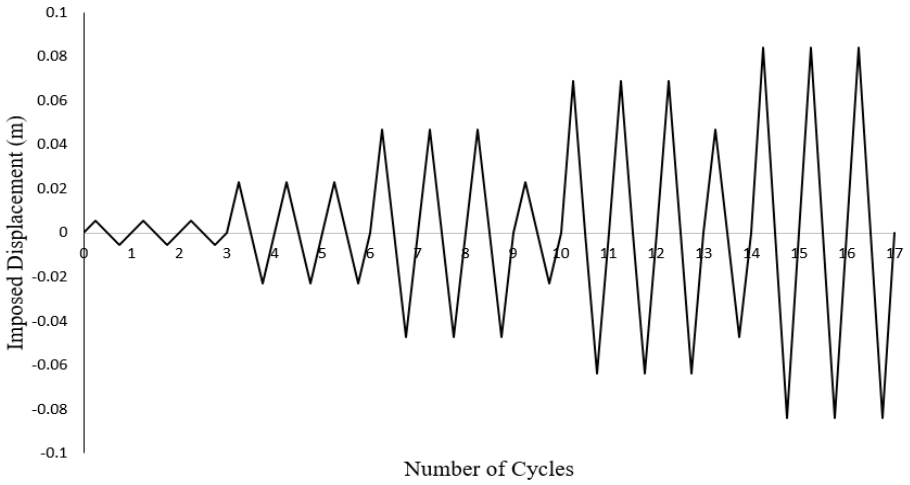

Fig. 15. Imposed displacement history at the top of the column.

The RC column was subjected to different cyclic loading conditions according to the experimental test. A compressive force of 600 kN was applied at the top section, where the loading history imposed, is presented in Fig. 15 in the form of imposed displacements (17 cycles). The concrete domain was discretized with 8-noded hexahedral finite elements and the steel reinforcement was discretized with the beam finite element. A total number of 24 concrete hexahedral (17.5cm x 17.5cm x 15cm) and 120 steel elements were used so as to discretize the RC column, as illustrated in Fig. 14b. In addition to that, 8-noded hexahedral finite elements (blue color) were used at the support and at the top of the column so as to simulate the boundary conditions of the specimen and to avoid any local failure.

The computed force-displacement curves are compared with the corresponding experimental data in Fig. 16. As it can be seen, the numerical results match very well with the experimental ones. The hysteretic curves were predicted with a satisfying accuracy, in terms of loading capacity, stiffness and energy dissipation.

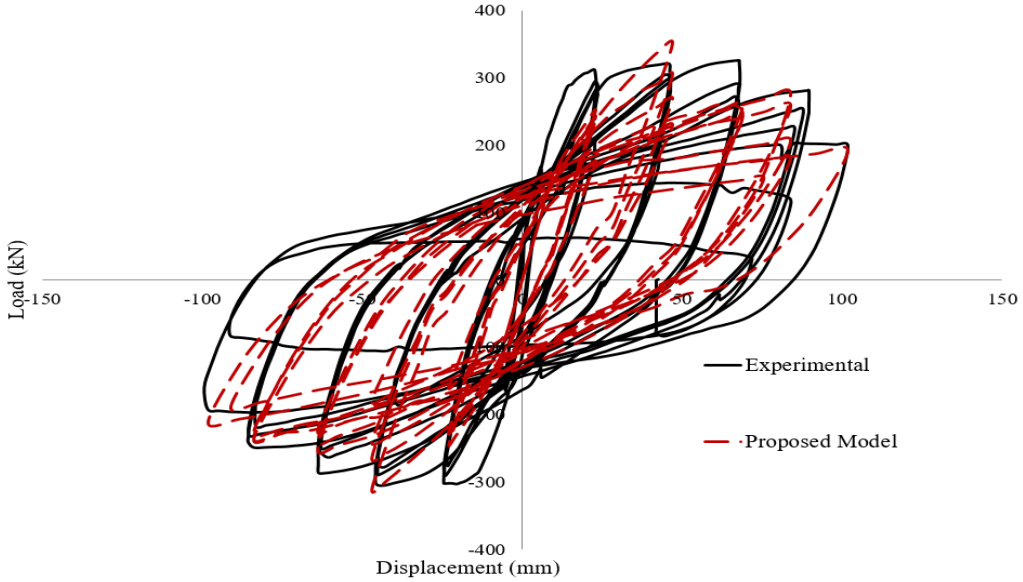

Fig. 16. RC Column. Comparison between numerical and experimental results.

Tables 9 and 10 show the comparison of the numerical and experimental results in terms of dissipating energy and load carrying capacity, respectively. The displacement level of the first three cycles was the yield displacement of the column section as a whole and was recorded during the test, where the rate of strain variation was very high at relatively constant loads. Experimentally the structure presents a hysteretic behavior with a dissipated energy close to 700 kN·mm, which

represents a mere 7.8% of the dissipated energy reported for the 4th loading cycle as shown in Table 9. In this case, the numerical model behaved elastically during the first three cycles, which represents a stiffer behavior. Table 9, shows that the numerical curves capture the corresponding experimental ones in terms of dissipating energy of the 4-17 cycles by an average value of 27%. It is also interesting to note here that, the deviation of the predicted energy dissipation drops to a 19% when accounting the last 9 loading cycles, where the damage level of the specimen is the highest. Furthermore, Table 10 shows that the load carrying capacity of the structural member was accurately predicted by an average value of 11%.

Table 9. Comparison of the dissipated energy between experimental results and the numerical model.

RC Column	Dissipated Energy Experimental (kN mm)	Dissipated Energy Predicted (kN mm)	Divergence from experimental (%)
4th Cycle	8921.82	3521.09	60.53
5th Cycle	6680.65	3521.09	47.29
6th Cycle	5893.46	3587.74	39.12
7th Cycle	21679.26	13221.18	39.01
8th Cycle	19298.80	14151.39	26.67
9th Cycle	18600.37	13836.27	25.61
10th Cycle	4508.34	3861.10	14.36
11th Cycle	34293.16	24124.29	29.65
12th Cycle	31069.46	25390.41	18.28
13th Cycle	27697.69	24537.60	11.41
14th Cycle	12729.03	12980.82	1.98
15th Cycle	44082.07	33610.14	23.76
16th Cycle	40108.10	32898.84	17.97
17th Cycle	37092.32	28281.42	23.75
		Average	27.10

Table 10. Comparison of the horizontal load of each cycle between experimental and numerical results of the proposed model.

RC Column	Horizontal Load Experimental (kN)		Horizontal Load Predicted Proposed (kN)		Divergence from Experimental	
	Positive	Negative	Positive	Negative	Positive (%)	Negative (%)
4th Cycle	311.90	-303.30	252.35	-245.88	19.09	-18.93
5th Cycle	294.60	-290.80	243.11	-228.47	17.48	-21.44
6th Cycle	283.00	-276.50	239.42	-224.31	15.40	-18.87
7th Cycle	321.00	-305.50	352.17	-312.87	9.71	-2.41
8th Cycle	304.60	-289.90	305.64	-265.86	0.34	-8.29
9th Cycle	298.40	-278.60	269.18	-241.86	9.79	-13.19
10th Cycle	205.50	-178.30	176.02	-161.20	14.34	-9.59
11th Cycle	325.90	-287.20	259.60	-252.98	20.34	-11.91
12th Cycle	291.60	-263.70	260.05	-240.97	10.82	-8.62
13th Cycle	271.40	-250.20	243.41	-225.34	10.31	-9.94
14th Cycle	204.30	-185.50	230.03	-181.40	12.59	-2.21
15th Cycle	281.50	-249.00	258.33	-235.07	8.23	-5.60
16th Cycle	253.50	-230.90	275.88	-227.43	8.83	-1.50

17th Cycle	226.50	-217.80	206.60	-237.85	8.79	-9.20
				Average	11.86	-10.12

During the last cycles, the numerical model exhibits failure of the longitudinal reinforcement, which also indicates the discrepancies of the last cycles in terms of dissipative energy. Nevertheless, the numerically predicted stiffness degradation is in a good agreement with the experimentally obtained curve.

The required Newton-Raphson internal iterations per displacement increment that resulted from the analysis of the RC column model are shown in Fig. 17. Once more, all displacement increments required a relatively low number of internal iterations to reach convergence despite the intense nonlinear behavior of the structure due to excessive shear cracking and rebar yielding. The iterative method in this case also used an energy convergence tolerance of 10^{-4}. As it can be observed in Fig. 17, 71% of the displacement increments required less than 15 internal iterations. The computational time for the nonlinear solution procedure of 780 displacement increments was 95 seconds (see Table 11). This numerical performance further confirms the computational efficiency of the developed algorithm.

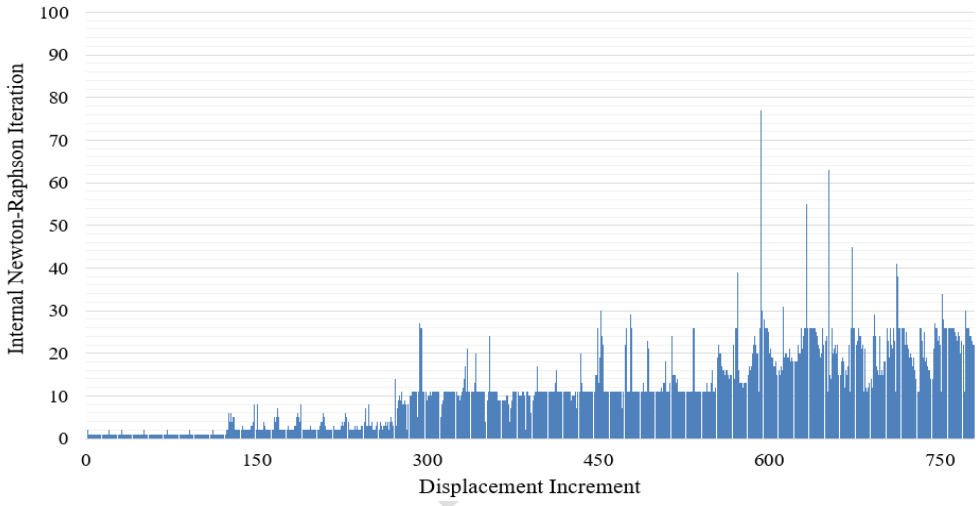

Fig. 17. RC Column. Required Newton-Raphson internal iteration per displacement increment.

Table 11. CPU time for different tasks of the nonlinear analysis for RC Column.

Task	CPU Time (s)
Embedded rebar element mesh generation	0.02
Nonlinear incremental-iterative solution	94.3
Total Time	94.32

4. Numerical Validation of the Proposed Model for Dynamic Analysis

4.1 Two-Storey RC frames

A numerical verification of the accuracy and computational efficiency of the proposed numerical method under dynamic loading will be performed on two two-storey RC frames (L30 and H30) that have been tested experimentally in [41]. The convergence tolerance was once more set to 10^{-4} for the Newton-Raphson iterations, while the nonlinear implicit Newmark integration method was used for the dynamic solution of the equations of motion. The steel rebars were simulated as embedded beam elements within the hexahedral concrete elements as presented in [31].

These two-storey frames were experimentally investigated by performing dynamic tests in an attempt to verify the validity of the European code provisions for the design of earthquake-resistant structures (Carydis [41]). The geometric and reinforcement details are shown in Fig. 18. The cylindrical specimen's uniaxial compressive strength of concrete (f_c) was 50 MPa and the yielding stress (f_y) of the steel reinforcement was 500 MPa. Additional masses of 2.87 and 2.62 tons were applied at the lower and upper levels, respectively.

Frame L30 was designed to exhibit moderately low ductility by using a behavioral factor of q = 2.5, whereas the frame H30 was designed to exhibit a higher ductility factor of q = 5. The frames were subjected to horizontal motions applied at their base, as denoted by the green vectors in Fig. 19. The base motions were sine-like acceleration records along the plane of the frames as illustrated in Figs. 20a and 20b. The accelerograms exhibit a maximum magnitude of approximately one and two times the magnitude of the design ground acceleration of the frames, which was 0.30g. Furthermore, the response spectrum diagram of each earthquake simulation of L30 and H30 specimens is illustrated in Figs. 20c and 20d, respectively. In order to show the severity of the ground motion (maximum ground acceleration was 0.75g), the spectra used for the design of the specimens (Eurocode 8 [42], soil type B) are also plotted in Figs. 20c and 20d. The maximum spectral accelerations for L30 are 2.164g and 4.374g for test1 and test2, respectively. For specimen H30, the corresponding maximum spectral accelerations are 2.153g, 4.373g and 4.514g for test1, test2 and test3, respectively.

For the modeling requirements, the concrete and rebars were modeled as described in section 3, whereas the full finite element mesh can be seen in Fig. 19. It is worth noting that the beam elements used to discretize the rebars have the exact location and direction of the actual reinforcement reported in [41]. The concrete mesh consists of 224 hexahedral finite elements (10cm x 15cm x 15.5cm) and 1,891 steel embedded beam rebar elements that were used to model the reinforcement of the L30 specimen. For the second specimen (H30), a total of 2,384 embedded rebar beam elements were used and the same number of hexahedral elements was used to discretize the concrete domain. For the discretization of the RC slabs, 128 8-noded hexahedral elements were used (red elements in Fig. 19), where the mass density of the elements was set accordingly in order to account for the additional mass placed on the structure.

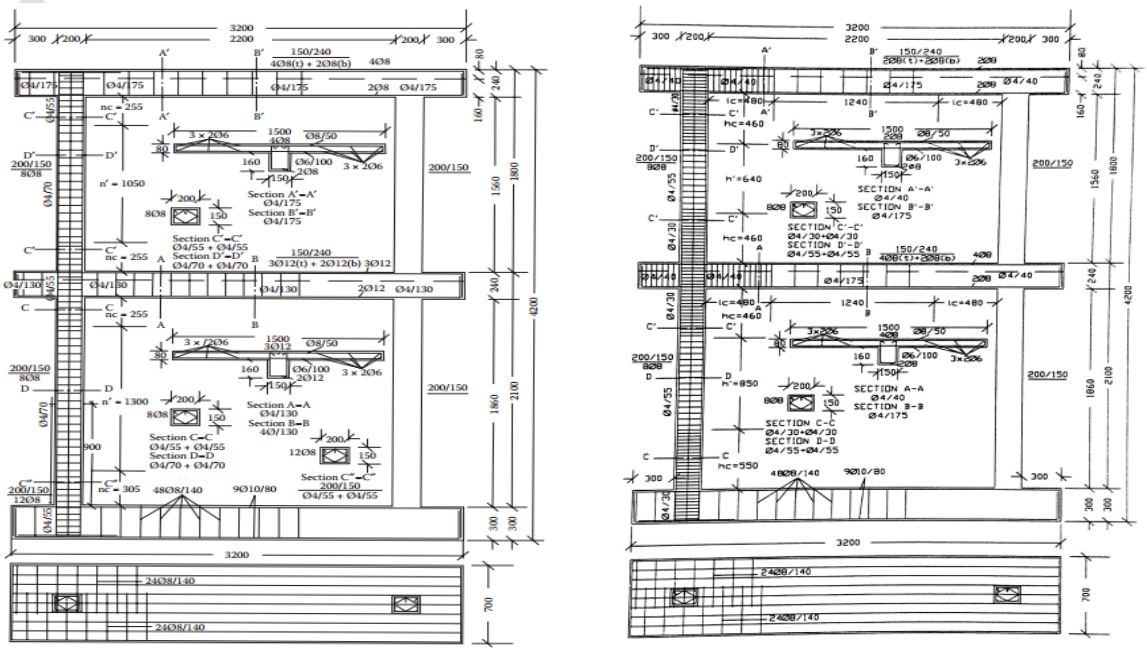

(a) (b)

Fig. 18. Geometric and reinforcement details of specimens of the RC-frames. (a) L30 and (b) H30.

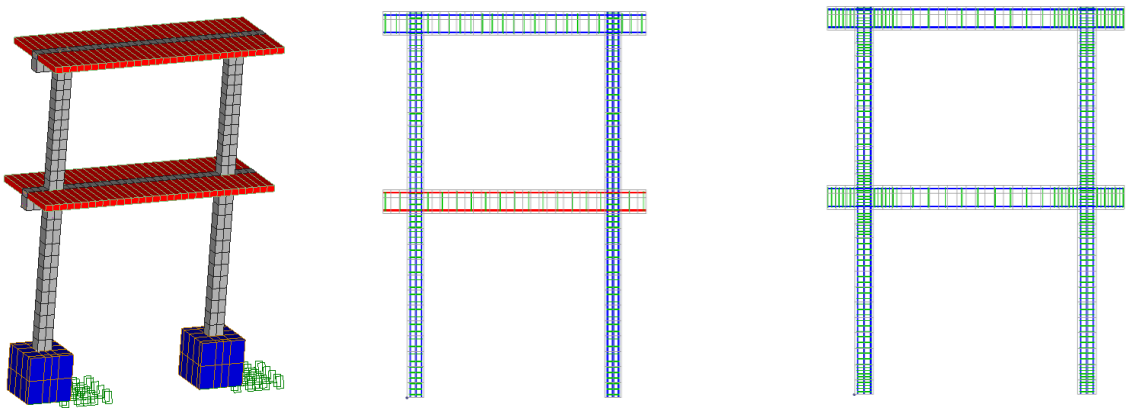

(a) (b)

Fig. 19. 3D view of the FE mesh of 8-noded hexahedral and embedded rebar elements (a) L30 and (b) H30.

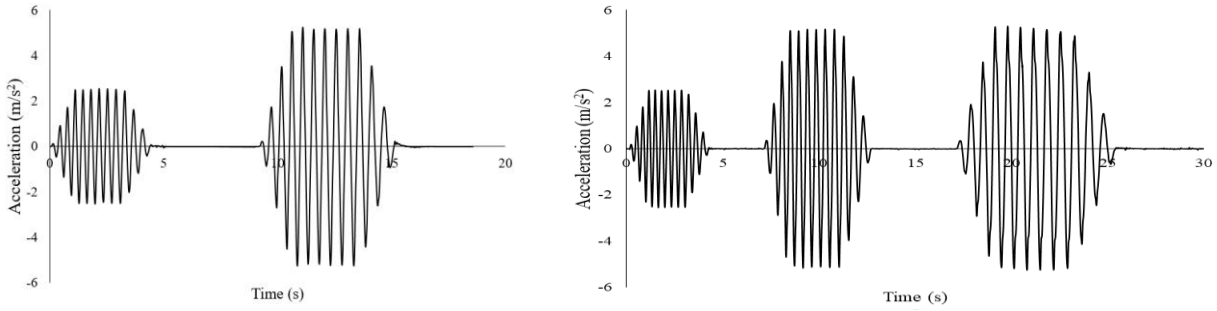

(a) (b)

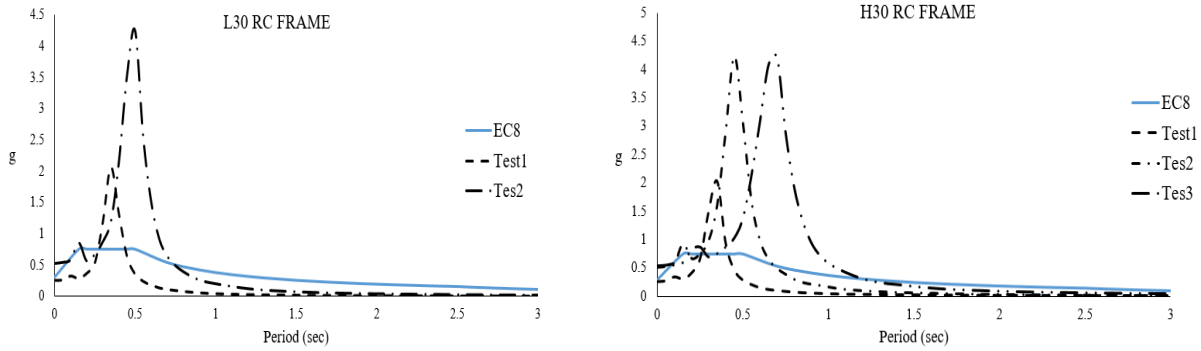

(c) (d)

Fig. 20. Base acceleration that were subjected during the experiments [35] and the numerical analyses of specimens (a) L30 and (b) H30. Spectrum acceleration diagrams of (c) L30 and (d) H30 loading histories.

The fundamental in-plane period of the L30 model was found to be T_1 = 0.2 s (undamaged frame), following a modal analysis performed prior to the dynamic analysis. For the dynamic analysis the time step was set to ΔT = 0,007746 s (which was the time step used for the experimental data). In order to further verify the performance of the numerical simulation, the natural frequencies for the first two modes were computed and found to be equal to f_1 = 2.93 Hz and f_2 = 9.7 Hz. These values were very close to the experimental ones reported in [41] f_{1exp} = 3.05 Hz and f_{2exp} = 9.8 Hz. Furthermore, a constant damping ratio of 2% was applied in order to take into account other dissipating mechanisms during the nonlinear dynamic analysis.

The numerically obtained curves, for the case of specimen L30, were compared with the experimental data as shown in Figs. 21-23. It is easy to observe that the numerical model managed to capture adequately the dynamic response of the structure in terms of story displacement time histories (see Figs. 21-23), demonstrating the ability of the proposed modeling method in capturing

the dynamic behavior of this low ductility frame well after the 8th second, where it had developed significant damages (see Figs. 21-23 dynamic response after the 8th second). Fig. 23 shows good agreement between the numerically computed and experimentally measured base shear of the frame.

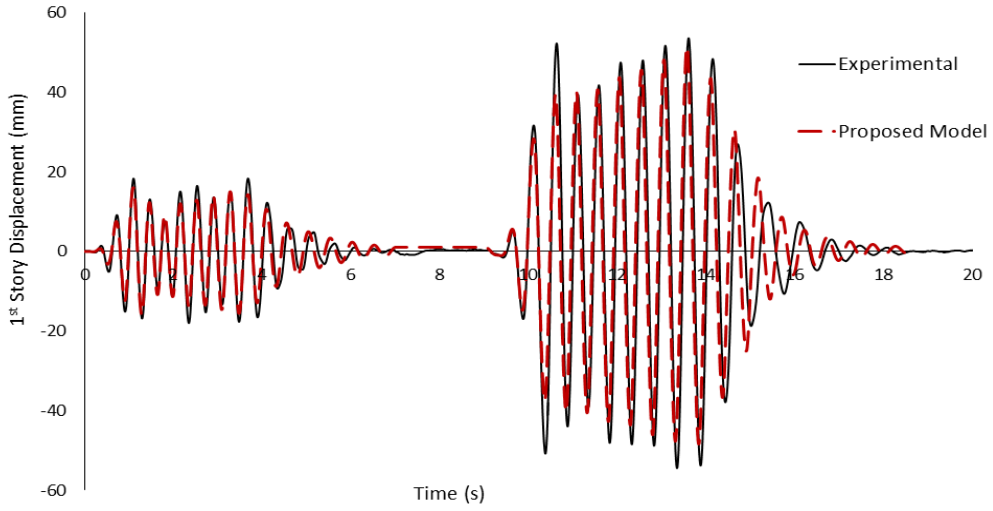

Fig. 21. L30 frame. Comparison between the numerical and experimental results of the 1st story displacement response.

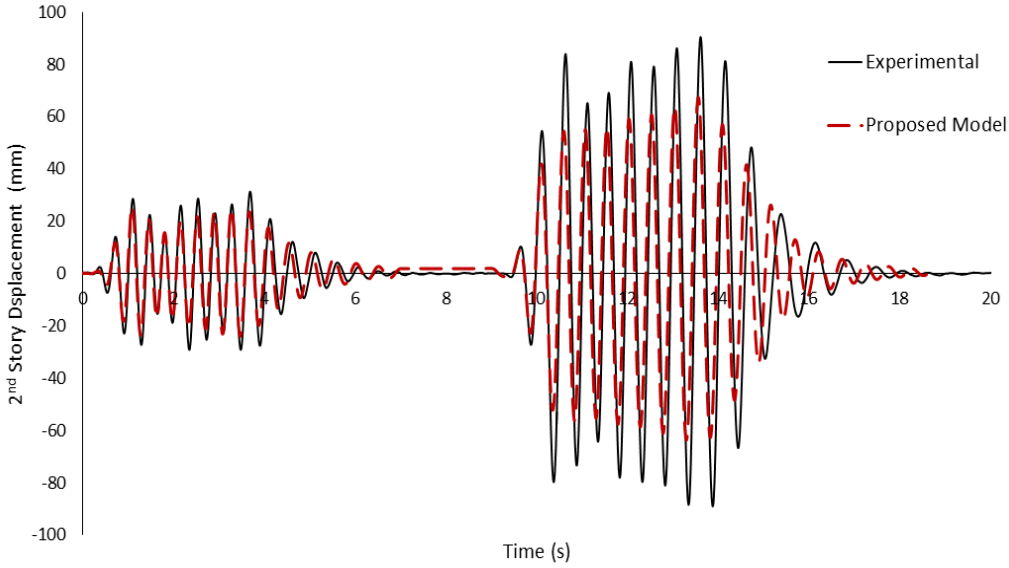

Fig. 22. L30 frame. Comparison between the numerical and experimental results of the 2nd storydisplacement response.

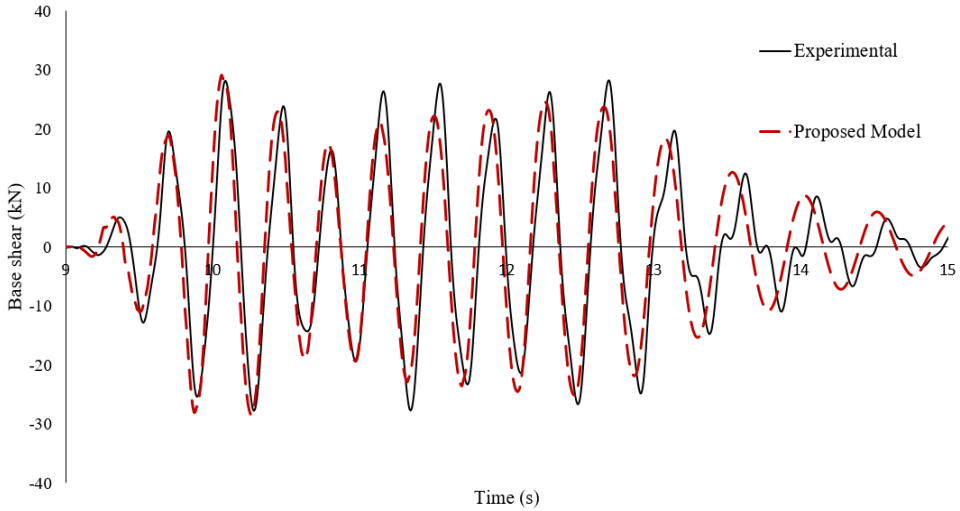

Fig. 23. L30 frame. Comparison between the numerical and experimental results of the base shear-time history during test 1.

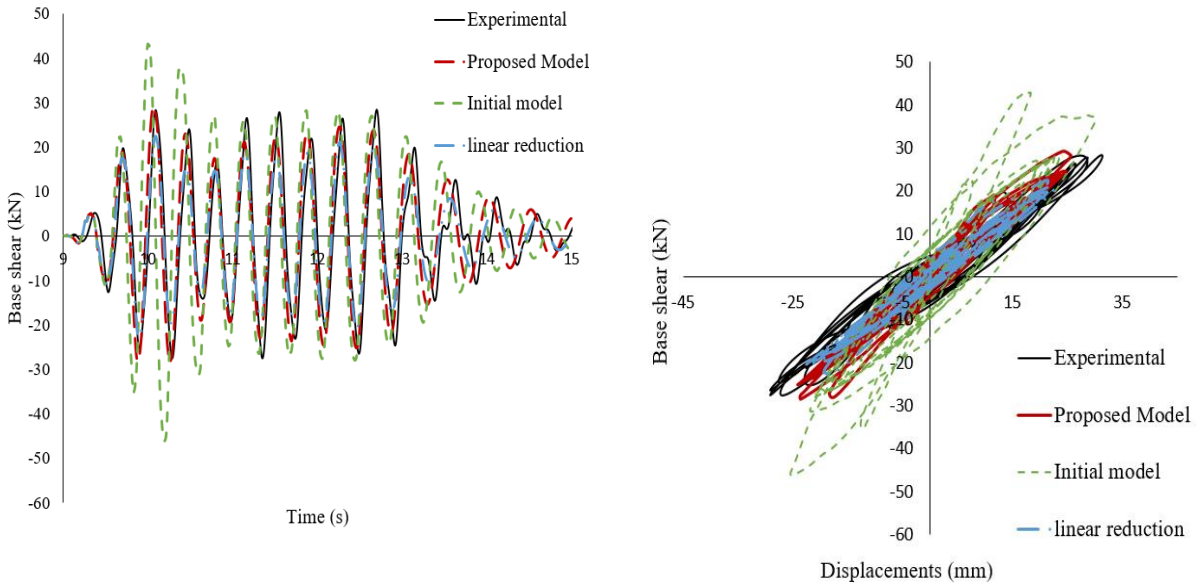

Fig. 24. L30 frame. Comparison between the numerical and experimental results of the base shear-time history for three different concrete damage factor formulations.

In an attempt to further investigate the proposed damage factors presented in this work, the L30 RC frame has been also analyzed with the "initial model" without activating the proposed damage factors. Another formulation of the proposed concrete damage factor was also explored in this numerical experiment by assuming a linear correlation between the damage factor D_{CL} and the parameters a, f_{CC}, ε_{cr}, ε_{max} (Eq. 18). This model is referred to as "linear reduction".

$$D_{cl} = \left[1 - \frac{1-a}{f_{cc}}\right] = \left[1 - \frac{\varepsilon_{cr}}{\varepsilon_{\max} \cdot f_{cc}}\right] \tag{18}$$

In Fig. 24, the numerical results for this test case are presented for the case of the three different models that were used during this parametric investigation. It can be seen that, the model with the linear reduction damage factor exhibited higher damages, thus lower base shear, in comparison to the corresponding model with the proposed concrete damage factor of Eq. 8. Hence, the "linear reduction" model derived a lower load-carrying capacity with a decreased hysteretic behavior. However, the numerical model without the damage factors exhibited a stiffer behavior during the first three dynamic cycles in comparison to the corresponding experimental results [41]. As a result, this model presented an excessive cracking at the beginning of the test, leading to premature damages that affected the overall dynamic behavior of the structure. This is attributed to the numerical inability of the model to absorb the developed energy that is generated during the initial dynamic cycles of the test. As a consequence, this led to discrepancies in terms of stiffness and displacements of the numerically predicted structural dynamic response.

The second test case was performed on H30 RC frame of Fig. 18b, which was designed in order to exhibit a more ductile behavior by adding more stirrups to the frame in comparison to the L30 specimen. The experimental and numerical tests revealed that, the frame developed excessive cracking, which occurred at the first dynamic cycles of the excitation (first 3 s of the experiment, see Fig. 25). This led to significant strength degradations mainly during the third round of dynamic loading (t > 17 s) as well as due to the yielding and fracture of the longitudinal reinforcement at the base of the frame, which was a behavior also observed during the experiment [41]. The numerically computed displacements of the first and the second floor slabs of the RC frame are compared with the experimental data in Figs. 25 and 26, respectively.

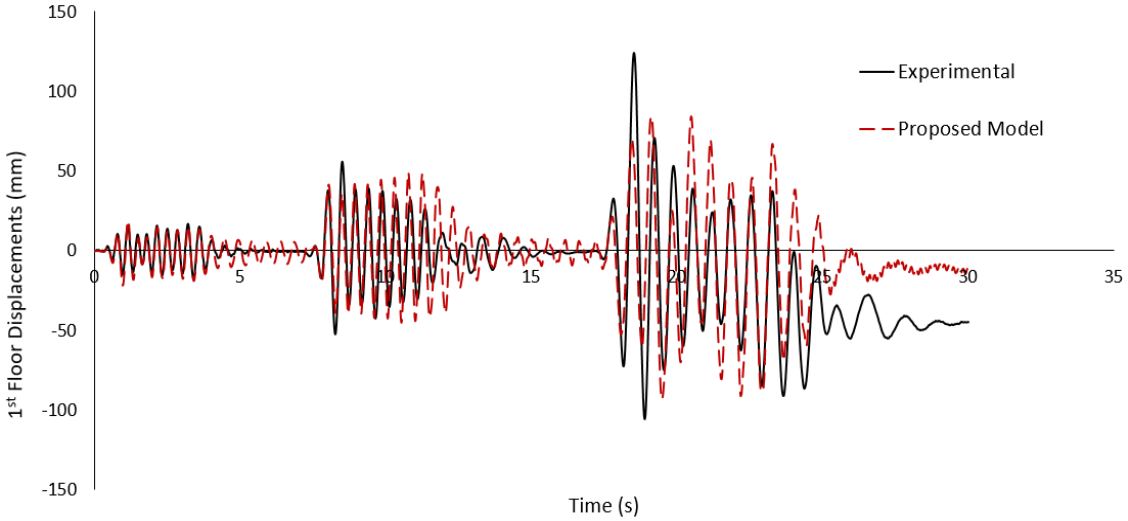

Fig. 25. H30 frame. Comparison between the numerical and experimental results of the 1st story displacement response.

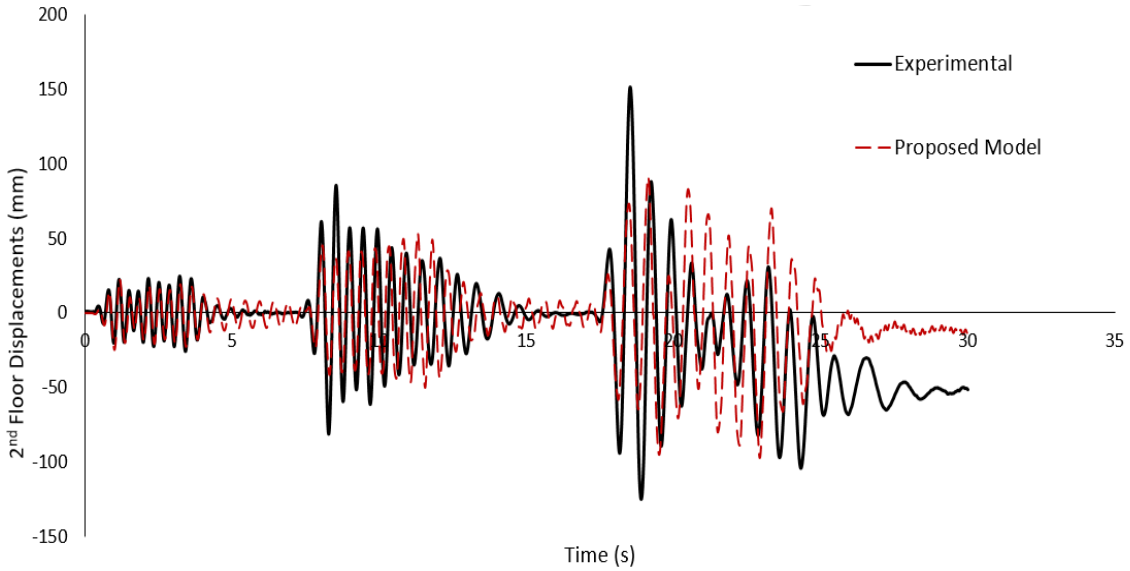

Fig. 26. H30 frame. Comparison between the numerical and experimental results of the 2nd story displacement response.

The numerical findings indicate that the proposed model managed to model the complete dynamic displacement history satisfactorily. It can be observed that during the first two sinusoidal acceleration events the response of the RC frame was predicted fairly accurately, while during the third sinusoidal acceleration event the experimental test exhibited a relatively stiffer behavior. Based on the experimental findings reported in [41], the frame developed severe damages at the base, thus the specimen practically failed due to excessive cracking and rebar failures. This was also the reason of the remaining deformation that can be noted during the last 5 seconds of the experiment (see Figs. 25 and 26). It is evident that the dynamic behavior of the H30 RC frame was governed, at that point, by extreme nonlinearities that forced the development of large horizontal deformations. Nevertheless, the numerical model manages to describe the overall behavior in a satisfactory manner, without any numerical instabilities.

It should be mentioned that, the computed fundamental in-plane period of the H30 model was found to be equal to T_1 = 0.22 s, while the same time step was used (ΔT = 0,007746 s) for the nonlinear dynamic analysis. The natural frequencies computed for the first and second modes were found to be equal to f_1 = 3.11Hz and f_2 = 14.31 Hz, respectively. These values were found to be close to the experimental ones reported in [41]: f_{1exp} = 3.28 Hz and f_{2exp} = 10.72 Hz.

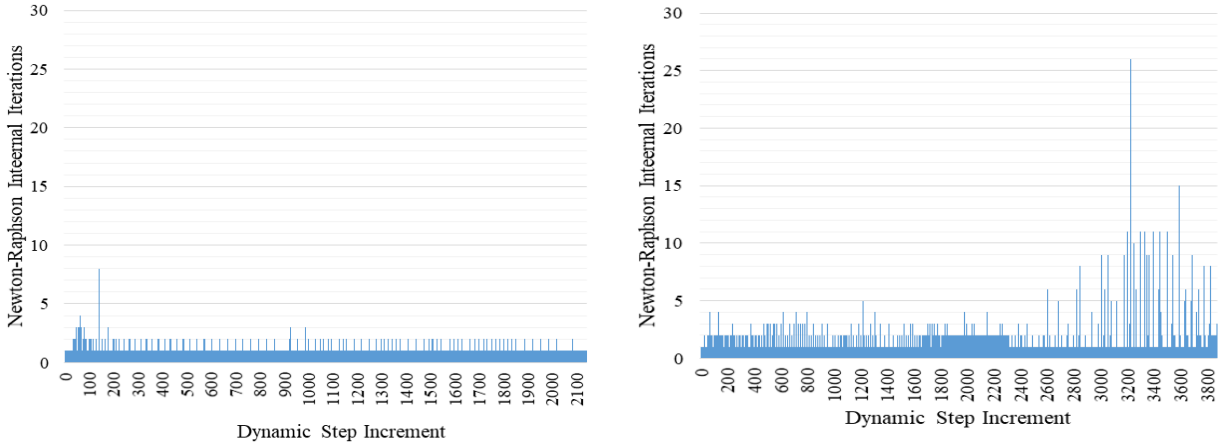

(a) (b)

Fig. 27. Required Newton-Raphson internal iterations per dynamic step increment (a) L30 and (b) H30.

The required internal iterations, for both L30 and H30 numerical models, are shown in the Figs. 27a and 27b. Throughout the numerical experiments, all the dynamic step increments required a reasonable number of iterations to achieve convergence regardless the degree of nonlinear behavior of the structures. From the computed numerical results, it was found that the required internal iterations per dynamic step during the solution procedure were limited to an average of 2 to 3, underlining the numerical stability of the proposed modeling method. For the L30 model, 87% of the dynamic steps require less than 2 internal Newton-Raphson iterations, while for the case of H30 a 78% of the dynamic steps required less than 5 internal iterations to achieve convergence. This increase is mainly attributed to the fact that during the 3rd sinusoidal acceleration event the analysis was governed by excessive nonlinearities due to significant cracking, rebar yielding and failure that was observed during the numerical analysis.

The computational times for the two nonlinear solution procedures are given in Table 12, which refer to the solution of 2,041 and 3,826 dynamic time increment steps for the test cases of L30 and H30, respectively. The total required time for solving the nonlinear dynamic problems was 319.5 s for L30 and 565.8 s for the case of H30.

Table 12. CPU time for different tasks of the nonlinear analysis for L30 and H30.

Task	L30	H30
	CPU Time (s)	CPU Time (s)
Embedded rebar element mesh generation	0.51	0.94
Nonlinear incremental-iterative solution	318.97	564.82
Total Time	319.48	565.76

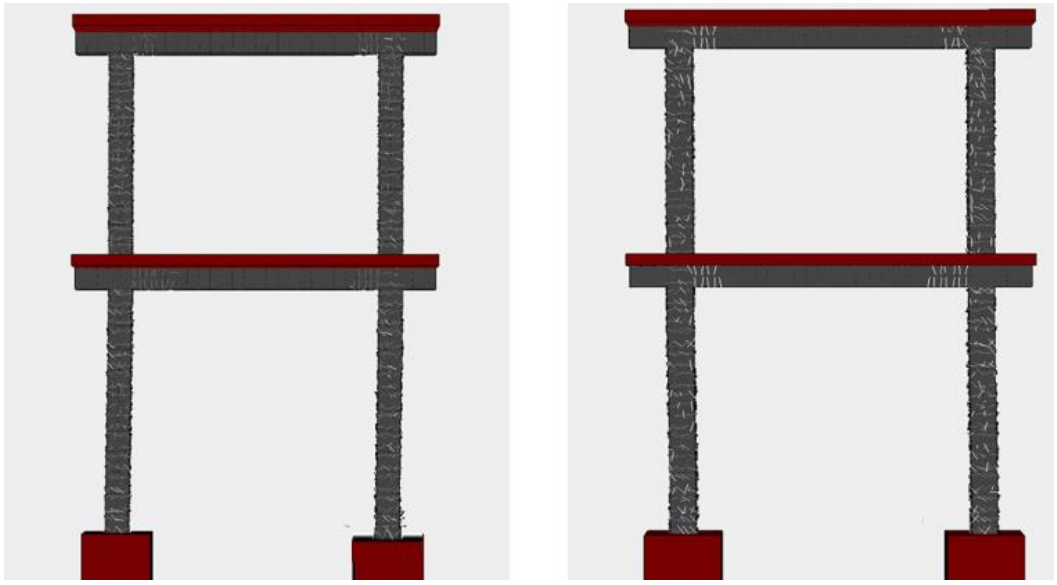

(a)

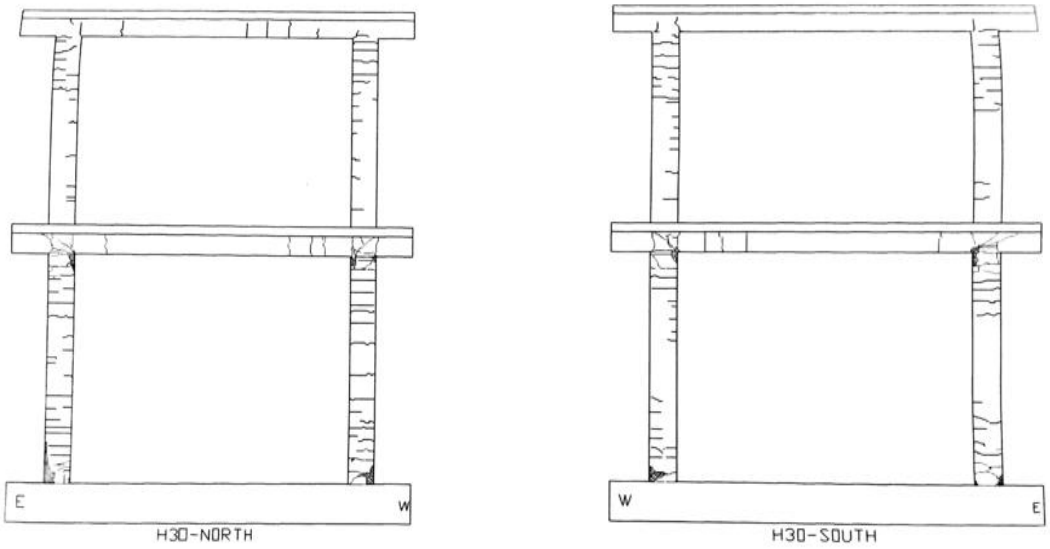

(b)

Fig. 28. H30 frame. Comparison between (a) numerical and (b) experimental obtained crack patterns.

Finally, Fig. 28 shows the crack patterns that were formed at the end of test 3 of the H30 frame. Based on the experimental observations [41], the cracks were mainly formed at the joints and the columns of the specimen. The cracks were larger and denser at the base of the frame, with significant inclination at the base of the first level. In this area, the experimentally observed damages were associated with intense concrete spalling. Similarly, intense inclination of the cracks appeared at the beam-column joints of the first level of the frame (ground floor). It can be seen that, there is a good agreement on the distribution, the location and the direction of the cracks, which are predicted by the numerical model compared to the corresponding crack patterns of the experimental test. However, the numerically predicted crack patterns appear to be denser than the experiment ones, which is again attributed to the adopted smeared crack approach.

4.1.1 Parametric investigation of using rod embedded elements

In this section, a comparison between the use of beam and rod elements for the simulation of steel reinforcement will be presented. The numerical model H30 is used to investigate the case where the rebars are modeled as embedded rods and compared to the numerical results obtained when beam elements are used for the rebar modeling. The same number of finite elements was used

in constructing the new model, whereas the material properties for both steel and concrete materials were also kept the same.

The comparison between the numerical results and the experiment, for the displacements of the second floor, is shown in Fig. 29. It can be observed that the model with the rod elements developed larger deformations due to the damage that was concentrated at the base of the structure during the 2nd sinusoidal acceleration event (t = 17 s). Therefore, the numerically predicted response during the 3rd sinusoidal acceleration event significantly deviate from the experimental results. As an overall conclusion in the case of this highly nonlinear dynamic problem, the use of beam elements provides additional numerical stability and accuracy to the dynamic simulation of concrete structures.

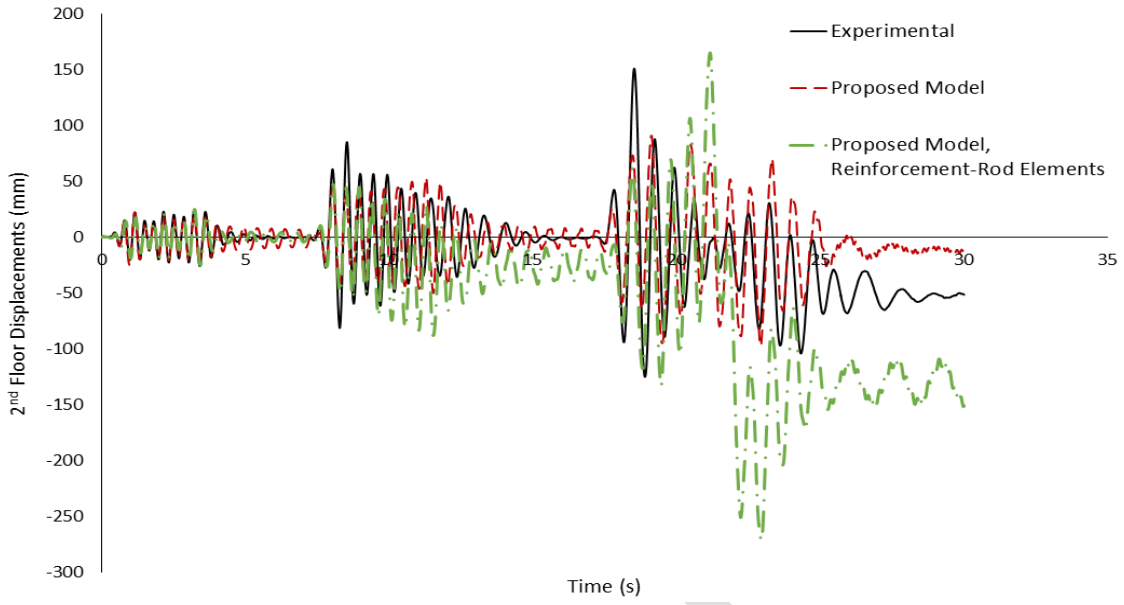

Fig. 29. H30 frame. Comparison between the numerical models that use rod and beam elements for modeling the rebars. Second story displacement history.

Table 13. CPU time for the nonlinear dynamic analysis of the H30 frame by using beam and rod elements for modeling the steel reinforcement.

Task	H30_Steel Reinforcement: Beam element	H30_Steel Reinforcement: Rod element
	CPU Time (s)	CPU Time (s)
Embedded rebar element mesh generation	0.94	0.71
Nonlinear incremental-iterative solution	564.82	534.36
Total Time	565.76	535.07

Table 13 shows the corresponding computational time required by the two models to solve the complete dynamic problem. As it can be seen, the model with rod elements is only 5% faster than the corresponding model with the beams. This illustrates the numerical efficiency of the developed algorithm, where the additional computational cost with the beam finite element is practically negligible.

4.1.2 Investigation of a modified crack closure criterion

The crack closure algorithm applied in [3] performs the computation of the strains at a cracked Gauss point, where the corresponding strain is computed along the norm of the crack's plane without closing the other cracks existed at the same Gauss point. A modified criterion is examined in this section, where all cracks are assumed to close when the crack-closure condition is satisfied

at any direction of a Gauss point. In this way, more stiffness is induced in the numerical model when any crack is closing at a given double cracked Gauss point.

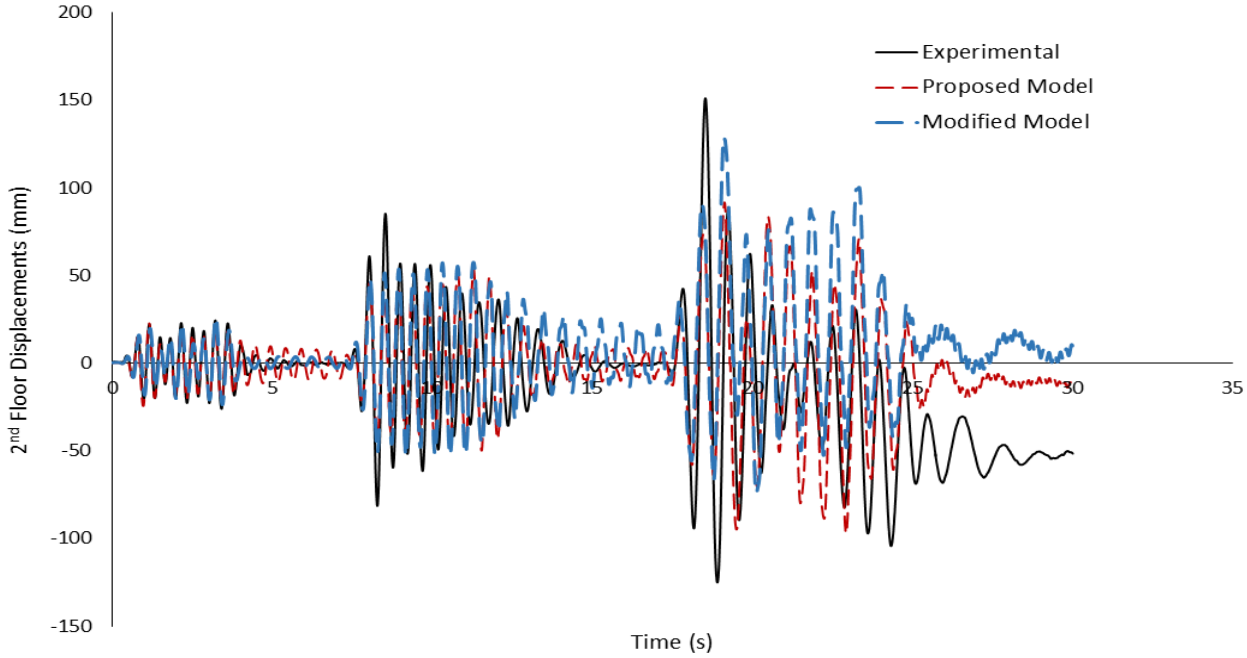

Fig. 30. H30 frame. Comparison between the numerical and experimental results of the second story displacement history of the proposed model and the modified model.

Fig. 30 shows the results from the dynamic analysis performed with the H30 frame, where the second level displacement history is depicted. The graph compares the curves that occurred from the use of the new crack-closure assumption described above and the model with the closing criterion described in [3]. The use of the modified criterion, exhibits a similar dynamic behavior with that obtained when using the standard crack-closure criterion, for the case of the first two sinusoidal acceleration events. The main changes are noted at the transition stage between the 2nd and 3rd events (see Fig. 30), where the stiffer numerical model (modified model) exhibits a deviation from the experimental data due to the additional stiffness added to the system. At this point, it is evident that the stiffer model (modified model) delivers significantly larger deformations in comparison to the model that uses the standard crack-closure criterion. During the dynamic analysis, it was also found that areas with lower crack numbers managed to close faster when unloading occurred, thus attracting more stiffness in comparison to other areas that did not manage to have their cracks closed. This numerical phenomenon had as a consequence the redistribution of the internal stresses between the cracked and uncracked regions of the structure which forced the frame to develop larger damages at the base of the frame during the 3rd and final cycle. Nevertheless, both models managed to capture the experimental results in a satisfactory manner, demonstrating the algorithm's ability to simulate complicated and challenging nonlinear dynamic problems.

4.1.3 Mesh-sensitivity Analysis

In order to examine the mesh sensitivity of the proposed modeling approach, four additional meshes were developed to model the L30 RC frame as shown in Fig. 31. The four meshes that were additionally developed for the needs of this parametric investigation (a, b, c and d in Fig. 31), consisted of 294, 318, 512 and 576 hexahedral elements, respectively. The numerical results were compared with the experimental data and the numerical results that derived from the model presented in Fig. 18, which consisted of 392 hexahedral elements.

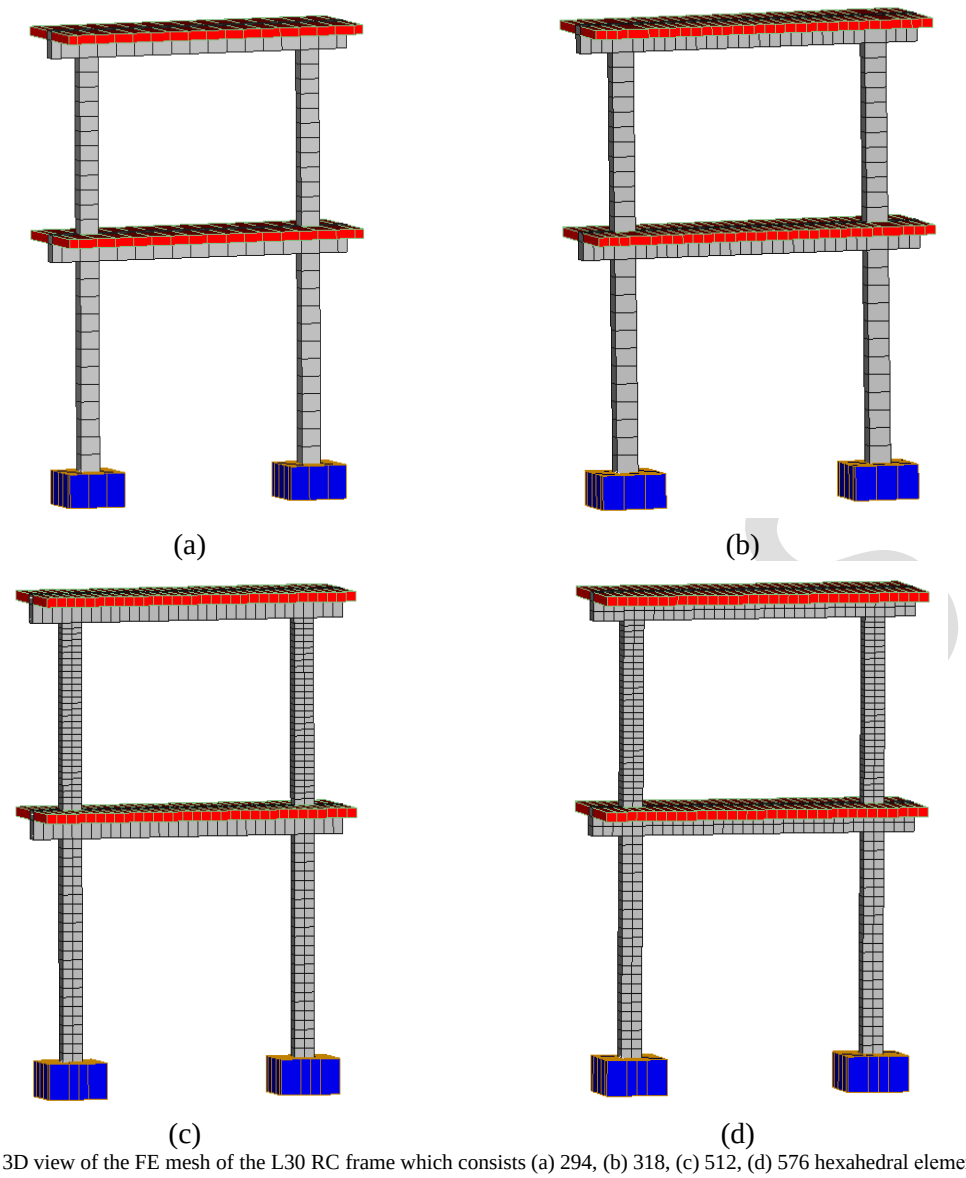

Fig. 31. 3D view of the FE mesh of the L30 RC frame which consists (a) 294, (b) 318, (c) 512, (d) 576 hexahedral elements.

After the dynamic analyses were performed, the obtained displacement curves were compared as it is illustrated in Fig. 32, where the numerically derived horizontal deformations of the second storey were plotted for the case of each developed mesh. It is easy to observe that the variations between the displacement responses that resulted numerically by the four different meshes are minimal, whereas all models managed to solve the complete nonlinear dynamic problem without any numerical instabilities. Furthermore, it is also easy to observe that, they all managed to capture the experimental data with a satisfactory accuracy. It is well known that, when a finer finite element mesh is used the overall nonlinear numerical behavior of a model is accordingly affected, a numerical phenomenon that can be also seen in Fig. 32, thus explains the small variations in terms of displacements between the different numerical models.

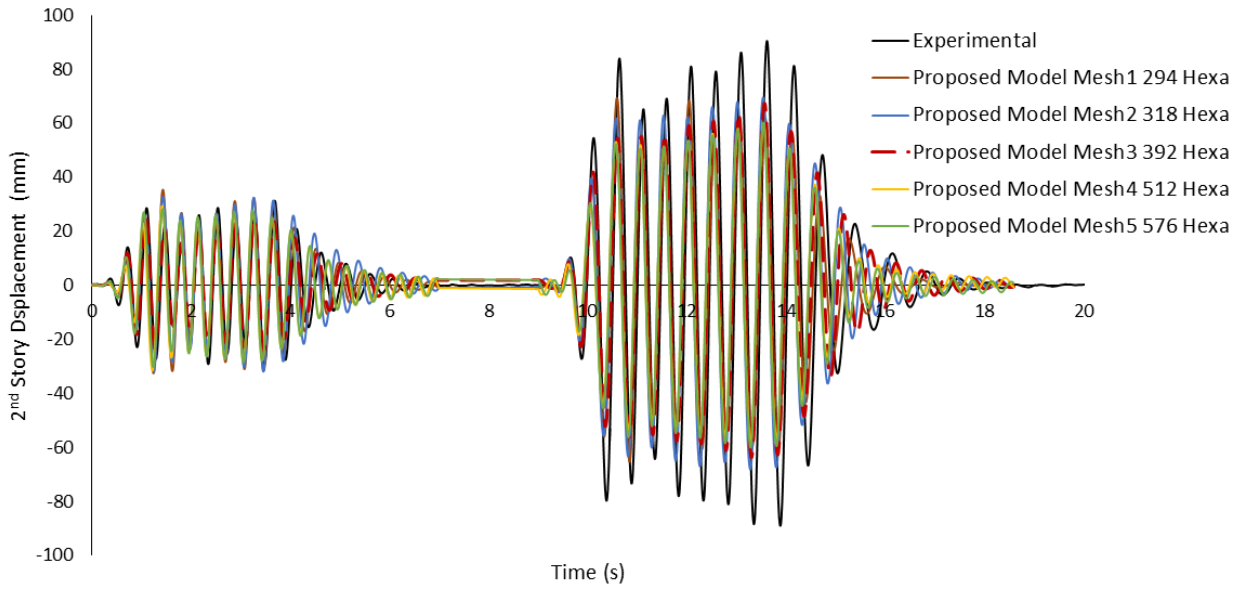

Fig. 32. Comparison between numerical and experimental results of the second story's displacement response for the different mesh discretizations.

It is evident that the first two models, which consist of 294 and 318 hexahedral elements, present slightly larger horizontal displacements given that their meshes foresee the discretization of the column section by using a single hexahedral element. Due to the coarser meshes adopted in these models (see Fig. 31a and 31b), the obtained numerical results exhibit a slightly larger stiffness due to the larger elements that are used to discretize the RC frame's columns, hence their dynamic response at the beginning of the dynamic excitation leads to the development of damages at an earlier stage in comparison to the models that adopt a finer mesh (crack openings). This phenomenon leads to a more brittle behavior, which eventually causes a relatively higher accumulated damage and consequently larger deformations during the dynamic excitation. However, it is safe to conclude that the numerical models derived negligible discrepancies, capturing the experimental results with an acceptable accuracy. It is also noteworthy to state at this point that the use of smaller finite element sizes in an attempt to further refine the RC frame's mesh would eventually add significant computational demand without any numerical merit. As it can be seen in Table 14, the computational demand to solve the complete nonlinear dynamic problem when the mesh with the largest number of finite elements is used, it requires approximately four time more computational time (13 min) than the model with the coarser mesh (3.3 min). This highlights the importance of developing a method that will be able to use a coarser mesh when dealing with a full-scale structure, without significantly decreasing its numerical accuracy. As it was previously stated, all numerical models were analyzed by using a standard computer system with a CPU power of 2,50 GHz.

So as to further investigate the numerical response that derives when the mesh size adopted for discretizing the RC frame changes, the first two natural frequencies were also computed herein and compared with the experimental data. Table 15, shows the natural frequencies that resulted from the five numerical models that were used in this mesh sensitivity study, where it can be seen that the maximum variation was 17.57% and 46.73% for mode 1 and 2, respectively. Both variation values derived from the coarser mesh, as it can be seen in the relevant table. This numerical phenomenon is attributed to the fact that the two models with the coarser meshes derive a stiffer numerical response at the beginning of the excitation and therefore they result higher natural frequency values. However, the overall average computed error values for the first two modes were

equal to 0.5% and 15.3%, respectively, a numerical finding that shows the ability of the proposed numerical method to reproduce the experimental data in a satisfactory manner.

Table 14. Computational demand resulted through the sensitivity analysis of the L30 frame.

Model	Number of Hexahedral Elements	CPU Time		
		Embedded rebar mesh generation (s)	Nonlinear Solution Procedure (s)	Total Time (s)
Mesh 1	294	0.37	198.1	198.47
Mesh 2	318	0.46	212.36	212.82
Mesh 3	392	0.51	318.97	319.48
Mesh 4	512	0.87	608.02	608.89
Mesh 5	576	0.99	774.33	775.32

Table 15. Natural frequencies resulted through the sensitivity analysis of the L30 frame.

Model	f_1 (Hz)	f_2 (Hz)	$\frac{f_1 - f_{1,exp}}{f_{1,exp}}$ (%)	$\frac{f_2 - f_{2,exp}}{f_{2,exp}}$ (%)
Experimental	3.05	9.8	-	-
Mesh 1	3.59	14.38	17.57	46.73
Mesh 2	3.30	14.11	8.33	44.00
Mesh 3	2.93	9.70	-3.93	-1.02
Mesh 4	2.80	9.31	-8.26	-5.04
Mesh 5	2.71	9.02	-11.24	-7.95
		Average	0.5	15.3

The numerical pathology of developing mesh-dependent constitutive models arises from the use of softening characteristics in the constitutive laws. Models usually use the smeared crack approach for simulating cracking thus avoid mesh discontinuities and remeshing procedures. This way, the models simulate the geometrical discontinuity through the assumption of displacement continuity. This procedure introduces excessive strains along the cracked areas. The constitutive models, which describe the post-peak behavior with descending branches, present some stiffness in these cracked areas that is not realistic (take for instance a tensile crack; along that direction the stiffness is zero but the descent branch assumes the contrary). A general numerical deficiency of the smeared crack approach, based on the Rots and Blaauwendraad work [43], is the possibility of developing stress-locking when smeared softening laws are applied, a numerical problem that is alleviated herein due to the brittle concrete behavior assumption. In continuation to that, Bazant and Oh [44] reported that excessive stress and strain concentrations in cracked areas lead to mesh-dependent procedures, thus the load needed to reach the strength limit strongly depends on the choice of element size and incorrectly converges to zero. Once again, this numerical phenomenon is not affecting the proposed method due to the fact that it does not foresee the use of a softening branch.

Most researchers proposed crack band models introducing the fracture energy [44], which is considered to be a material parameter. Additionally, nonlocal techniques have been investigated [26] which are usually combined to damage models. Finally, second-order gradient-based methods have also been proposed. Rots et al. [45] replaced the softening diagram of the constitutive laws to a saw-tooth diagram of positive slopes. A series of limiter analyses (“event-by-event strategy) replace the incremental Newton-method and led to robust results, as it was reported by the authors [45]. On the other hand, the proposed material model of this work, describes the concrete behavior as a brittle material with an abrupt loss of its caring capacity when the failure criterion is satisfied during the nonlinear dynamic analysis. Therefore, the numerical model manages to discharge the

cracked areas from the prementioned excessive stress concentrations by releasing them to the surrounding uncracked areas, thus, the numerical instabilities are in this case prevented, hence the proposed method leads to a mesh-independent numerical procedure.

In addition to the above, it was also observed that during the nonlinear dynamic analysis of the L30 RC frame, in some cases where finer meshes were used so as to numerically study the dynamic response of the specimen, the sections of the columns that are found at the base of the frame developed significant cracking due to the large bending moments that were developed during the numerical experiment. The steel-reinforcement elements take in this case the role of the post-cracking behavior of concrete within the hexahedral elements that have embedded rebars, while the hexahedral elements that do not contain any embedded rebars are called to resist to the external forces without the tensile resistance capacity of the steel rebars. This phenomenon is presented when finer meshes are used which may lead to local failures and divergence of the iteration solution procedure from an early stage of the analysis. This is a numerical phenomenon that is common when 3D detailed modeling is used to solve problems that are expected to exhibit extreme nonlinearities [46], where the effect of cracks are modeled either through the use of the smeared crack approach or through damage models. Additionally, a more extensive mesh sensitivity investigation was performed and presented in [46], where deep RC beams without stirrups were modeled under monotonic loading conditions.

According to the numerical investigation performed and presented in this section, it was found that the use of 10-20 cm hexahedral elements ensure a reliable element size that can be used for establishing numerical efficiency, robustness and accuracy. In addition to that, the overall numerical findings discussed in this section show that by developing a numerical method that exhibits numerical accuracy and robustness when coarser meshes are implemented, it further highlights that the nonlinear dynamic simulation of full-scale RC structures with 3D detailed models is now feasible.

4.2 RC frame

A final test case shown in Fig. 33, was selected to further study the efficiency of the proposed algorithm. The RC space frame denoted as frame W050, was investigated by Minowa et al. [47]. The RC frame consists of four columns, which were fixed on a shake table at their lower-end and monolithically connected to a steel rigid slab at the top. The columns had a height of 850 mm and a square cross section of 130x130 mm. The geometric details of the RC specimen are given in Fig. 33. The uniaxial compressive strength (f_c) of concrete is 26 MPa and the yielding stresses (f_y) of the steel reinforcement are 380 and 392 MPa for the 16 and 6 mm in diameter rebars, respectively. The spacing of the stirrups for each of the four columns is 50 mm, where the total mass placed on the roof is 27.8 tons. The RC frame was subjected to one-dimensional excitations along its longitudinal axis of symmetry. The imposed acceleration record at its base is illustrated in Fig. 34, where after the 15^{th} second, the structure undergoes accelerations that increase through time, forcing the frame to develop a significant nonlinear behavior [47]. Thus, the numerical results that will be presented herein will therefore concentrate on the dynamic behavior of the structure after the 15^{th} second of the dynamic excitation.

The concrete domain was modeled by 8-noded hexahedral finite elements and the steel reinforcement were modeled with beam elements. The transverse and longitudinal embedded rebar elements had the exact location and direction of the actual reinforcement. The top and the bottom of each RC column are modelled with 96 rigid 8-noded hexahedral elements in order to avoid local

failure that maybe developed at these regions. Overall, 48 concrete finite elements (6.75cm x 13cm x 15cm) and 368 embedded rebar elements were used to model the four RC columns.

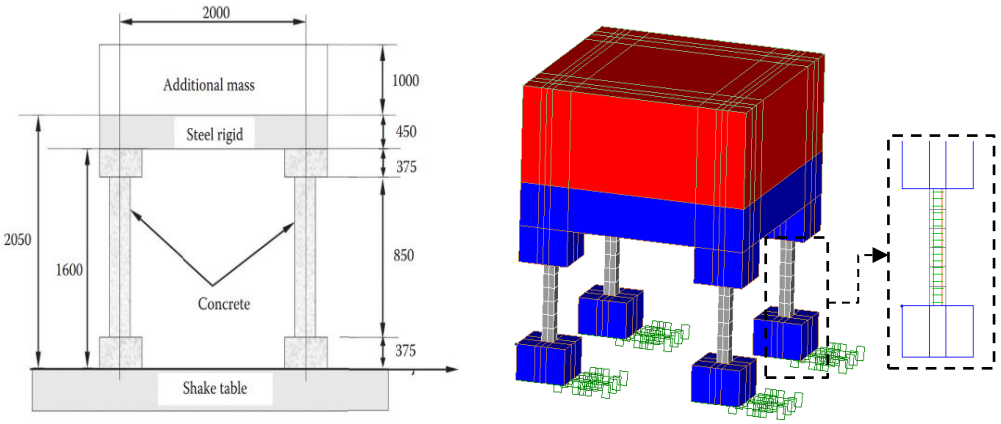

Fig. 33. W050 RC frame. Geometric details [47] and FE mesh with solid and beam finite elements.

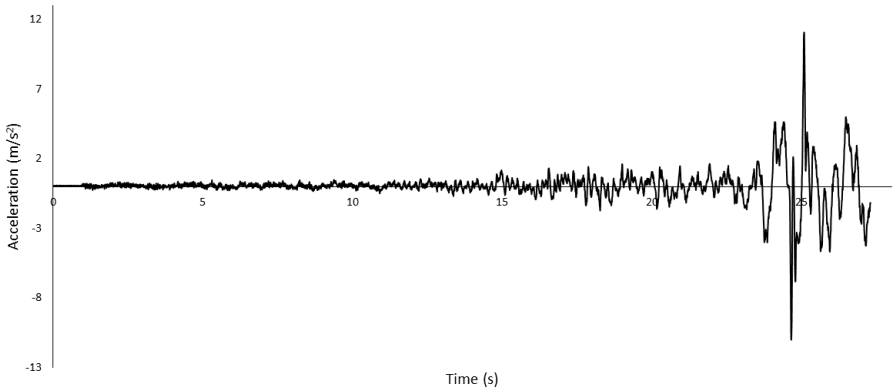

Fig. 34. W050 RC frame. Base acceleration of the shake table.

For the steel slab and the additional mass applied at the top of the specimen, 126 hexahedral elements were used to construct the mesh. After performing a modal analysis, it was found that the fundamental period computed by the numerical model was equal to $T_1 = 0.17$ s, a numerical result obtained by using the undamaged properties of the concrete and steel materials. Therefore, the dynamic time integration step was set to $\Delta T = 0.005$ s for the needs of the nonlinear dynamic analysis. The numerical curves are compared with the experimental data in Figs. 35 and 36.

The obtained results indicate that the numerically predicted displacements are in a good agreement with the experimental data (Fig. 34), while during the final stages of the numerical experiment ($t > 24$ s) the model exhibited high damages at the base of the frame, resulting into larger deformations in comparison to the experiment test [47]. This can be attributed to the highly nonlinear response after the development of significant cracking and spalling at the base of the structures. By comparing the numerical and experimental base-shear in Fig. 36, it can be seen that the numerical model is able to capture the overall behavior of the specimen with a satisfactory accuracy, while the deviation of the curves is more pronounced after the 26th second of the analysis.

It is important to state at this point that the experiment [47] reported significant damages at the columns leading to an actual collapse of the structure. This indicates that the experimental measurements beyond the 24th second of the dynamic excitation could be hindered by a lack of accuracy given the significant nonlinearities that led to the instability of the frame and subsequently to the development of very large deformations. It is widely accepted that measuring accurately the dynamic behavior of any structure which exhibits nonlinear behavior is a challenge on its own, thus many things can affect the final measurements during an experiment. It is therefore impossible for

any numerical simulation to be able to capture the experimental results with an absolute accuracy due to numerous reasons, such as lack of additional information regarding the specimen, experimental errors during measurements, external factors that affect the execution of the experiment, as well as the inability of the numerical model to capture additional physical phenomena that take place when rebars start to fail. On the other hand, when dealing with the objectivity and ability of the numerical model to produce the same results when modeling the same specimen, it is evident that the risks involved are significantly lower in comparison to those involved in a physical experiment.

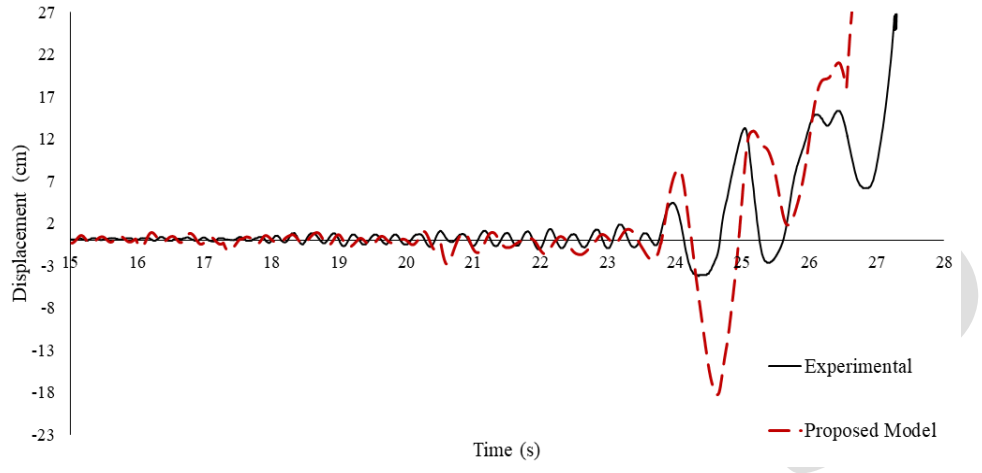

Fig. 35. W050 RC frame. Comparison between numerical and experimental results of the displacement response.

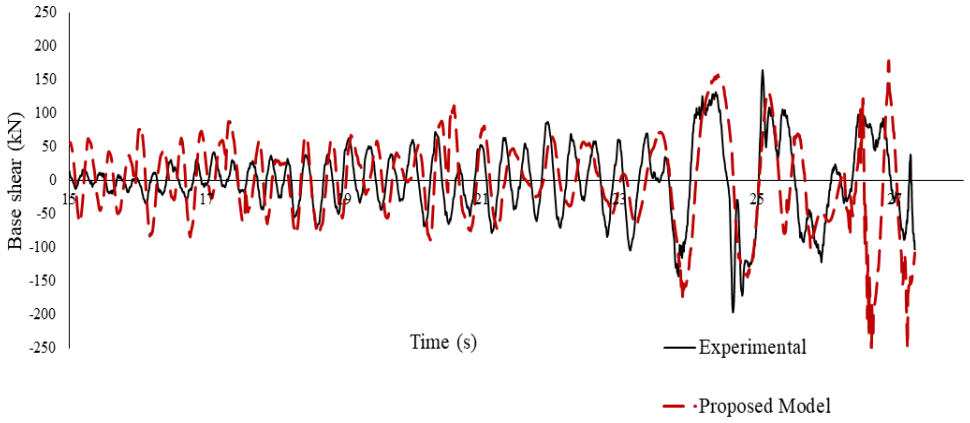

Fig. 36. W050 RC frame. Comparison between numerical and experimental results of the base shear response.

a)

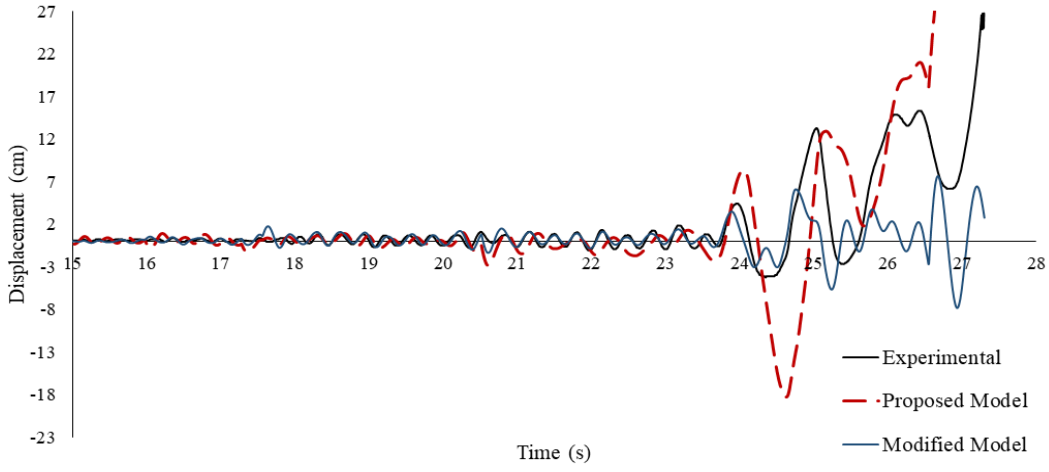

b)

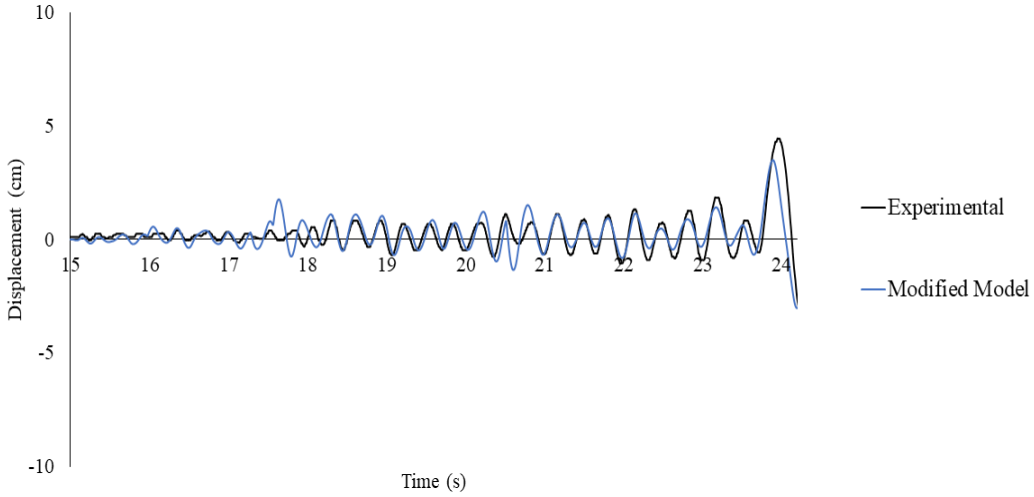

Fig. 37. W050 RC frame. a) Comparison between numerical and experimental base shear curve for the case of modified model and the proposed model. b) Comparison between numerical and experimental base shear curve for the case of modified model during the 15th and 24th seconds.

In an attempt to further study the proposed algorithm, the RC frame model was also tested with the modified crack-closure procedure that was described in section 4.1.2. Fig. 37 shows the results of the numerically predicted displacement history. The comparison shows that the modified model derived displacements that were more accurate than the model with the initial crack closure criterion during the dynamic excitation between the 15th and 24th seconds of the numerical test (Fig. 37b). This numerical finding occurred due to the excessive cracking that occurs during this period using the initial crack closure criterion. However, after the 24th second the proposed model managed to capture more realistically the behavior since the vertical displacements were increased significantly and in a similar manner to that of the experiment [47]. On the other hand, the stiffer behavior when the modified model is used, leads to smaller horizontal deformations at the final stage of the dynamic excitation, thus not being able to capture the failure that occurred at the completion of the dynamic excitation. The computational time for solving the complete dynamic problem was measured and presented in Table 16. It can be seen that, the total required time for performing 5,459 dynamic increments, (with a total of 6,636 internal iterations) was 726 seconds, illustrating the computational efficiently of the proposed algorithm. In addition to that, the required internal Newton-Raphson iterations during the solution procedure are given in Fig. 38, where it can be observed that most of the increments required a mere 1 to 2 internal iterations to achieve convergence, demonstrating the numerical stability of the proposed method when dealing with ultimate limit state dynamic loading conditions.

Table 16. CPU time for different tasks of the nonlinear analysis for the W050 RC Frame.

Task	CPU Time (s)
Embedded rebar element mesh generation	0.07
Nonlinear incremental-iterative solution	725.3
Total Time	725.37

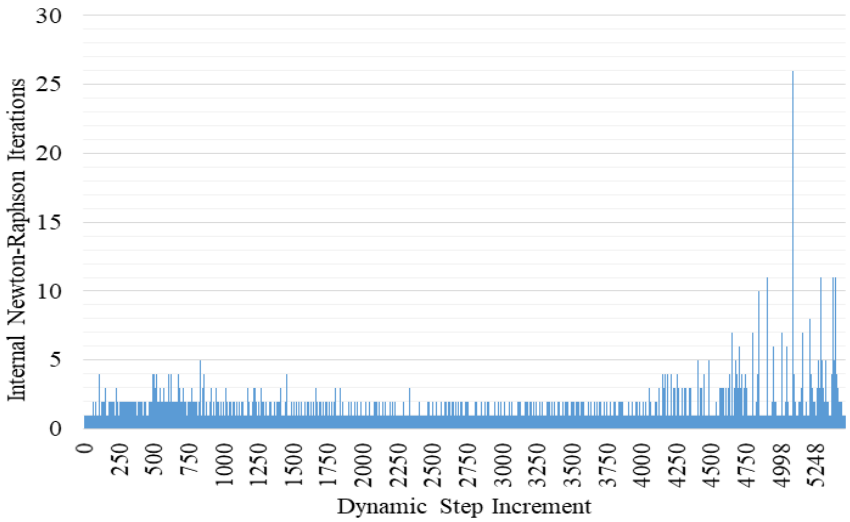

Fig. 38. W050 RC frame. Required Newton-Raphson internal iterations per dynamic step increment.

5. Conclusions

In this research work, the integration of a 3D detailed solid finite-element model with damage factors related to both concrete and steel reinforcement was proposed for the nonlinear static cyclic and dynamic analysis of RC structures. The concrete material constitutive model combines a realistic assumption of the behavior of concrete, which numerically perfectly fits with the smeared crack approach. The numerical model with crack opening and closing introduced in [3], has been integrated with a proposed concrete damage factor that was formulated by using the characteristics of cracking during the nonlinear cyclic analysis as well as by a damage factor for the steel material model that is also directly connected to the number of opening and closing of concrete cracks, leading to an accurate and numerical efficient algorithmic implementation.

An extensive numerical investigation was performed in order to validate the ability of the proposed modeling framework to capture the cyclic static and dynamic response of RC structures. To achieve this objective, three different experimental setups were modeled and analyzed under ultimate limit state of nonlinear static cyclic loading conditions, while three RC specimens where studied under dynamic loading excitations. All selected experimental setups have been subjected to cyclic loads that forced the structural elements to develop extreme nonlinearities and multiple crack openings and closings.

In the case of structures tested for static cyclic loading, the proposed model was found to be able to capture the level of damage caused by the crack opening and closing, as reported in the various experiments and to predict the overall behavior of the specimens with computational efficiency. Based on the numerical findings, the overall contribution of the proposed damage factors for concrete and steel were found to be crucial for being able to add numerical stability to the overall numerical solution process, as well as for capturing phenomena such as the pinching effect. The numerical study revealed that the steel damage factor was crucial in the case of static cyclic loading.

Regarding the dynamic tests performed under ultimate limit state conditions, the proposed damage factors were found to play a crucial role during the dynamic analysis of the structures contributing to the ability of the proposed modeling approach to predict the experimental data. Based on the numerical investigation conducted on the RC frame H30, it was concluded that the use of beam elements, is a more realistic simulation approach for the steel reinforcement, which improves the numerical results compared to the experimental data. When the rod embedded rebars are used, the H30 frame model was found to develop larger horizontal deformations during the 3rd

sinusoidal acceleration event compared to the experimental response. Furthermore, a mesh sensitivity analysis was performed and discussed in section 4.1.3 for the case of the L30 frame model. The analysis concluded that the proposed modeling approach manages to capture the experimental results without any significant mesh sensitivity effects. Based on this numerical investigation, it was also concluded that the developed algorithm managed to solve all nonlinear dynamic problems without any numerical instabilities and at the same time exhibited high computational efficiency, which is a crucial characteristic when dealing with the solution of large-scale structures.

A numerical investigation was also performed with a modified crack-closure algorithm, where all cracks were assumed to close when any of the two cracks was found to be closing at a Gauss point. This modified approach had a negligible effect on the numerical response during the first two sinusoidal acceleration events (H30 RC frames). However, in the 3rd dynamic test the effects of the crack-closure assumption were greater, but still managed to capture the overall dynamic behavior of the under study frame, without any numerical discrepancies. This sensitivity analysis demonstrates that the proposed algorithm is not affected by modifications related to the crack opening and closing mechanism. The same crack-closure assumption was studied in section 4.2 for the W050 RC frame, where the numerical findings indicated that the modified approach was suitable when the structure is heavily cracked but it delivered a stiffer behavior at the end of the experiment. When the structure was subjected to high dynamic excitations and began to fail, the modified approach overestimated the structure's stiffness.

In conclusion, the numerical results presented in this work, demonstrated the ability of the proposed algorithm to capture experimental results with severe nonlinearities, while the numerical model implemented for the simulation of the nonlinear 3D behavior of RC structures was characterized by a reduced computational effort that makes the proposed numerical simulation appealing for the analysis of large-scale structures undergoing excessive cyclic static and dynamic loading [48].

ACKNOWLEDGEMENTS

The financial support provided by the European Research Council Advanced Grant "MASTER-Mastering the computational challenges in numerical modeling and optimum design of CNT reinforced composites" (ERC-2011-ADG 20110209) is gratefully acknowledged by the authors. The authors would like to acknowledge M.D. Kotsovos, P.G. Carydis, K.V. Spiliopoulos and G.Ch. Lykidis for providing the experimental data of the analysis of the RC structural members.

References

[1] Markou G., Papadrakakis M. (2013), "Computationally efficient 3D finite element modeling of RC structures". Computers and Structures, 12(4), 443–98.

[2] Kotsovos, M.D. (2015), "Finite-Element Modelling of Structural Concrete: Short-Term Static and Dynamic Loading Conditions", CRC Press.

[3] Mourlas Ch., Papadrakakis M. and Markou G., "A computationally efficient model for the cyclic behavior of reinforced concrete structural members", Engineering Structures, 141, 97-125, 2017.

[4] Pagnoni T., Slater J., Ameur-Moussa R., Buyukozturk O. (1992), "A Nonlinear Three-Dimensional Analysis of Reinforced Concrete Based on a Bounding Surface Model", Computers and Structures, 43(1), 1-12.

[5] Ozbolt, J. and Bazant, Z.P. (1992), "Microplane model for cyclic triaxial behavior of concrete", Journal of Engineering Mechanics -ASCE, 118, 1365-1386.
[6] Eligehausen R., Genesio G., Ozbolt J.,Pampain S. (2009), "3D analysis of seismic response of RC beam-column exterior joints before and after retrofit", Taylor & Francis Group, London, ISBN 978-0-415-46850-3.
[7] Darwin, D. and Pecknold, D.A. (1977), "Analysis of cyclic loading of plane R/C structures", Computers and Structures, 7(1), 137-147.
[8] Balan, T.A., Filippou, F.C. and Popov, E.P. (1997), "Constitutive model for 3D cyclic analysis of concrete structures", Journal of Engineering Mechanics - ASCE, 123,143-153.
[9] Kwon, M. and Spacone, E. (2002), "Three–dimensional finite element analyses of reinforced concrete columns", Computers and Structures, 80, 199-212.
[10] Girard, C. and Bastien, J. (2002), "Finite Element bond slip model for concrete columns under cyclic loads", Journal of Structural Engineering- ASCE, 128, 1502-1510.
[11] Palermo, D. and Vecchio, F.J. (2002), "Behaviour of 3d RC shear walls", ACI Struct. J., 99, 81-89.
[12] Belletti, B., Cerioni, R. and Iori, I. (2001). "Physical approach for reinforced-concrete (PARC) membrane elements". Journal of Structural Engineering, 127(12), 1412-1426.
[13] Belletti, B., Scolari, M. and Vecchi, F. (2017) "PARC_CL 2.0 crack model for NLFEA of reinforced concrete structures under cyclic loadings", Computers and Structures, 191, 165–179.
[14] Richard B., Ragueneau F., Cremona C,Adelaide L. (2010), "Isotropic continuum damage mechanics for concrete under cyclic loading:Stiffness recovery, inelastic strains and frictional sliding", Engineering Fracture Mechanics, 77, 1203–1223.
[15] Jason, L., Huerta, A., Pijaudier-Cabot, G. and Ghavamian, S. (2006). "An elastic plastic damage formulation for concrete: Application to elementary tests and comparison with an isotropic damage model". Computer methods in applied mechanics and engineering, 195(52), 7077-7092.
[16] Yuchuan L., Shaoqian X., Xuechao G. (2011), "An Energy-based Damage Model for Concrete Structures under Cyclic Loading", Procedia Engineering, 14, 460–469.
[17] Inoue, N., Yang, K. and Shibata, A. (1997), "Dynamic nonlinear analysis of RC shear wall by fem with explicit analytical procedure", Earthquake Engineering and Structural Dynamics, 26, 967-986.
[18] Cela J. J. L. (1998), "Analysis of reinforced concrete structures subjected to dynamic loads with a viscoplastic Drucker±Prager model", Applied Mathematical Modelling, 22, 495-515.
[19] Kwan, W.P. and Billington S.L. (2001), "Simulation of structural concrete under cyclic load", Journal of Structural Engineering- ASCE, 127, 1391-1401.
[20] Ile, N. and Reynouard, J.M. (2000), "Nonlinear analysis of reinforced concrete shear wall under earthquake loading", Journal of Earthquake Engineering, 4(2), 183-213.
[21] Han T.S., Billington S.L., Ingraffea A.R., Simulation strategies to predict seismic response of RC structures. Finite Element Analysis of RC Structures, Willam K, Tanabe T (eds). ACI International, Farmington Hills, MI, 2001;ACI-SP-205-10:191–213.
[22] Mirzabozorg H. and Ghaemian M., "Nonlinear behavior of mass concrete in 3d problems using a smeared crack approach", Earthquake Engineering and Structural Dynamics 2005; 34:247–269

[23] Mazars J., Kotronis P. and Davenne L. (2002), "A new modelling strategy for the behaviour of shear walls under dynamic loading", Earthquake Engineering and Structural Dynamics; 31:937–954.
[24] Faria R., Oliver J. and Cervera M. (2004), "Modeling material failure in concrete structures under cyclic actions", Journal of Structural Engineering, 130(12):1997–2005.
[25] Richard, B. and Ragueneau, F. (2013). "Continuum damage mechanics based model for quasi brittle materials subjected to cyclic loadings: Formulation, numerical implementation and applications". Engineering Fracture Mechanics, 98, 383-406.
[26] Pijaudier-Cabot G., Bazant Z. (1987) "Nonlocal damage theory", Journal of Engineering Mechanics,113,1512–33
[27] Vassaux, M., Richard, B., Ragueneau, F., and Millard, A. (2015). "Regularised crack behaviour effects on continuum modelling of quasi-brittle materials under cyclic loading", Engineering Fracture Mechanics, 149, 18-36.
[28] Spiliopoulos, K.V. and Lykidis, G.C. (2006), "An efficient three dimensional solid finite element dynamic analysis of reinforced concrete structures", Earthquake Engineering and Structural dynamics, 35, 137-157.
[29] Cotsovos M. D., (2013), "Cracking of RC beam/column joints: Implications for the analysis of frame-type structures", Engineering Structures, 52 131-139.
[30] Moharrami, M. and Koutromanos, I. (2017) "Finite element analysis of damage and failure of reinforced concrete members under earthquake loading", Earthquake Engineering and Structural Dynamics, 1-20.
[31] Markou, G. and Papadrakakis, M. (2012), "An efficient generation method of embedded reinforcement in hexahedral elements for reinforced concrete simulations", Advances in Engineering Software ADES, 45(1), 175-187.
[32] Willam K. J. and Warnke E. P., (1974), "Constitutive model for the triaxial behaviour of concrete", Seminar on concrete structures subjected to triaxial stresses, Instituto Sperimentale Modeli e Strutture, Bergamo, Paper III-1.
[33] Menegotto, M., and Pinto, P. E. (1973). "Method of analysis for cyclically loaded reinforced concrete plane frames including changes in geometry and non-elastic behavior of elements under combined normal force and bending." Proceedings, IABSE Symposium on Resistance and Ultimate Deformability of Structures Acted on by Well Defined Repeated Loads, Lisbon, Portugal, 15–22.
[34] Kinugasa, H, Nomura, S. (1994), "Failure mechanism under reversed cyclic loading after flexural yielding", JCI Concrete Research and Technology, 5(2), 21–32
[35] Fenwick, R.C., Megget, L.M. and Wuu, P. (1996), "Load deflection characteristics of plastic hinges in ductile concrete beams", In Proceedings 11th WCEE.
[36] Kwak, H.G. and Kim, D.Y. (2004), "Material nonlinear analysis of RC shear walls subject to cyclic loading", Engineering Structures, 26, 1423-1436.
[37] Mansour, M.Y. and Hsu, T.T.C. (2005), "Behavior of reinforced concrete elements under cyclic shear. I: Experiments", ASCE Journal of Structural Engineering, 131(1), 44–53.
[38] Del Toro Rivera, R. (1988). "Behavior of reinforced concrete beam column joints under alternated loading", Ph.D. thesis, Ecole Nationale des Ponts et Chaussées, Paris.
[39] Shiohara, H. and Kusuhara, F., 2006, Benchmark Test for Validation of Mathematical Models for Nonlinear and Cyclic Behaviour of R/C Beam–Column Joints, Department of Architecture, School of Engineering, University of Tokyo.

[40] Saatcioglu, M., and Ozcebe, G. (1989), "Response of Reinforced concrete columns to simulated seismic loading", ACI Structural Journal, 86(1), 3-12.
[41] Carydis, P., (1997), "Shaking table tests of R.C. frames, ECOEST PPREC8", Report 8, 182.
[42] Eurocode 8 (2003), Design of structures for earthquake resistance.
[43] Rots, J.G. and Blaauwendraad, J. (1989), "Crack models for concrete: Discrete or smeared? Fixed, multidirectional or rotating?" HERON Journal, 34(1), 1-59.
[44] Bazant Z.P. and Oh B. (1983), "Crack band theory for fracture of concrete", RILEM Materials and Structures, 16, 155–177.
[45] Rots, J. G., Belletti, B. and Invernizzi, S. (2008). "Robust modeling of RC structures with an "event-by-event" strategy", Engineering Fracture Mechanics, 75(3-4), 590-614.
[46] Markou, G. and AlHamaydeh, M. (2017), "3D Finite Element Modeling of GFRP-Reinforced Concrete Deep Beams without Shear Reinforcement", International Journal of Computational Methods, 15(1), 1-35.
[47] Minowa, C., Ogawa, N., Hayashida, T., Kogoma, I. and Okada, T.(1995), "Dynamic and static collapse tests of reinforce-concrete columns", Nuclear Engineering and Design, 156, 269–276.
[48] Markou, G. and Papadrakakis, M. (2015), "A Simplified and Efficient Hybrid Finite Element Model (HYMOD) for Non-Linear 3D Simulation of RC Structures", Engineering Computations, 32(5), 1477-1524.